A Study of the Cosmic Ray Rate in the CHIPS-M Prototype Detector

A thesis submitted in partial fulfillment of the requirement
for the degree of Bachelor of Science in Physics from
The College of William and Mary

by

Brandon Taylor Kriesten

Accepted for HONORS
(Honors or no-Honors)

Patricia L. Vahle
Patricia Vahle Ph.D., Director

Gina L. Hoatson
Gina Hoatson Ph.D., Physics

Pietro Paparella Ph.D., Mathematics

Williamsburg, VA
April 30, 2015

A Study of the Cosmic Ray Rate in the CHIPS-M Prototype Detector

Brandon Kriesten*, Patricia Vahle*

Abstract

Following the discovery of neutrino mass and neutrino oscillations, the next big question is whether or not neutrinos violate charge-parity symmetry. To achieve the precision in electron neutrino appearance necessary to make measurements of charge parity symmetry violation, we need a detector with a very large fiducial mass. These large detectors are beyond our budgetary reach and take an incredible amount of time to build. The CHIPS collaboration is building a series of prototype detectors with the aim to lower the cost of these massive detectors and develop an incremental approach so that the physics measurements can be made in all phases of the program. To lower the costs, the detectors will be deployed under the water in an existing mine pit. An underwater detector design relieves the need to build a site to house the detector, provides an overburden of water to block many cosmic rays, and structurally supports the detector.

* *Department of Physics, The College of William and Mary: Williamsburg, VA. 23187*

Contents

1 Introduction

CHIPS-M is the modular test phase of the collaborative CHIPS (CHerenkov detectors In mine PitS) program utilizing water Cherenkov technology. This detector was deployed in the Wentworth mine pit in Soudan, Minnesota in August 2014. During the summer (May - August) of 2014, I worked on constructing and commissioning the detector, eventually deploying it into the flooded mine pit. Throughout this process I was involved in various aspects of the project such as general construction, plumbing, power cables, data analysis, and much more. The detector that I built during the summer was used for this honors thesis to investigate the cosmic ray rate and the environmental effects inside the CHIPS prototype detector.

2 Theoretical Introduction

2.1 A Brief Glimpse at the History of the Neutrino

Neutrinos were first postulated on December 4, 1930 by Wolfgang Pauli in his historic letter to the Physical Institue of the Federal Institute of Technology in Zurich entitled "Dear Radioactive Ladies and Gentlemen." In this letter, he claimed the existence of a new elementary particle called the "neutron" later to be known as the "neutrino". His neutral particle with spin-1/2 would explain the energy conservation violation seen in the electron energy spectrum of beta decay experiments. Instead of just one well-defined energy as theory predicted, the electron had a distribution of energy which was not explainable at the time. Enrico Fermi, after attending this conference, postulated a theory in 1934 in which these "neutrinos" are emitted with the electron [15]. The neutrinos emitted in the beta decay reaction contain the rest of the missing energy.

The first experimental observation of a neutrino was not made until 1953 when Reines and Cowan made the first measurements for electron antineutrinos using a detector near the Savannah River nuclear plant [5]. To find the neutrinos, Cowan and Reines investigated the inverse beta decay reaction, given by

$$\nu^* + p \rightarrow e^+ + n \tag{1}$$

$CdCl_2$ was loaded into a liquid scintillator to be used as the target in this experiment. The positron

emitted in this process will annihilate with an electron, quickly resulting in a release of energy in the form of gamma rays. Cowan and Reines found that the two gamma rays produced from the annihilation process each had an energy of approximately 0.51 MeV. If the neutron also created is captured by a Cd nucleus, it releases a gamma ray delayed by approximately $5\mu s$. The coincidence of both of the gamma ray events followed by a delayed gamma ray from the capture was the sign of an antineutrino formation. F. Reines would later win the Nobel Prize in Physics in 1995 for his discovery of the neutrino. Sadly, Cowan died before he could be recognized for his contribution [1].

In 1962 a new neutrino flavor, the muon neutrino, was observed at the Brookhaven Alternating Gradient Synchrotron (AGS). The muon neutrino was discovered through the decays of pions into muons and its corresponding neutrino. The experiment collided protons into a target to produce a shower of pions. The pions were redirected towards a muon stopper made out of old steel battleship parts. As the pions travelled toward the plates, they decayed into muons and muon neutrinos. The muons were stopped by the solid mass of the steel, but the muon neutrinos passed through the wall into a neon filled spark chamber. As the muon neutrinos interacted with the aluminum plates in the spark chamber, they exchanged a W boson and a muon was created. The muon passed through the spark chamber and a distinctive muon spark trail was created [4]. The experimental result of the existence of muon type neutrinos led to the idea that with each lepton, there is a corresponding neutrino flavor which is distinct from the other neutrino. The lepton group was then defined as the muon, the electron, and the corresponding neutrinos and anti-particles [8].

The tau lepton was not discovered until much later in 1978, due to it's heavier mass of 1776.8 MeV, by SLAC (Stanford Linear Accelerator Center). The tau was recognized as a heavier version of its lepton counterparts, the muon and the electron. From the decay of the tau, they saw a similar non conservation energy distribution as in the beta decay in 1930. It was hypothesized that the energy must have been carried off by a neutrino given the non conservation of energy in beta decay. A new flavor of neutrino was proposed to complement the symmetry so far predicted in the lepton group, the tau neutrino [16]. However, the tau neutrino remained hidden from experimental confirmation until 2000 when the DONUT Collaboration at Fermilab produced their experimental results [1].

2.2 Solar Neutrinos

From the early 19th century, many scientists have guessed at what fuels the sun. Some ideas advocated for gravity only, and some for radioactivity. In 1938, quickly following the discovery of the neutrino, a model of fusion reactions called Solar Standard Model (SSM) was suggested as the possible fuel source of the sun based off of the sun's thermodynamics and geometry. These reactions, dubbed the PP and CNO chains, create electron flavor neutrinos. Each chain produces only neutrinos within a specific energy threshold given the SSM predictions. The estimated flux of these neutrinos was also calculated given the luminosity of the sun.

In 1968, the collaboration of Ray Davis and John N. Bachall's experiment in the Homestake mine in South Dakota published the results of the detection of these solar electron flavor neutrinos using a chlorine based experiment. In Homestake, the electron neutrinos interacted in 100,000 gallons of tetra-chlorethylene and created radioactive Argon and an electron. This interaction required an electron neutrino energy threshold < 0.814 MeV (from the SSM), thus only neutrinos from the decay of Boron-8 in the PPIII solar fusion process were accepted. The radioactive Argon produced had a half life of approximately 25 days; thus, they could measure the amount of Argon in the detector and determine the flux of the electron neutrinos. In their results, only a third of the expected number of neutrinos were detected, a deficit of 69%. This is known as the solar neutrino problem [9].

The Gallium Experiment (GALLEX) and the Soviet-American Gallium Experiment (SAGE) also investigated this phenomenon. Both experiments used Gallium as a target to produce Germanium, an interaction with a much lower electron neutrino energy threshold (< 0.233MeV) meaning that neutrinos from all chains of nucleosynthesis could be accepted. The fluxes measured separately by each collaboration were in good agreement; however, they both differed from the Solar Standard Model with a 49% deficit.

An experiment known as Super Kamiokande confirmed these results in 2001. Super Kamiokande is a 22.5 kilo-ton fiducial mass water cherenkov detector located in the Kamioka Observatory in Japan. In their data, they observed "significantly lower solar neutrino fluxes than predicted by standard solar models" [6]. Super Kamiokande's detector is sensitive to electron type neutrinos, but not as sensitive to tau and muon flavors. With their experiment, they published a result of

45% of the expected flux of electron neutrinos.

Sudbury Neutrino Observatory (SNO) used a similar experiment of a 1 kilo-ton detector sitting in a flooded cavity in the Earth. Their detector was filled with D_2O or heavy water which allowed them to specifically look at interactions of electron, muon, and tau flavored neutrinos. Their experiment was designed to use electron scattering (both neutral current mode and charged current modes), charged current interactions, and neutral current interactions. SNO found that when accounting for all three neutrino flavors, the total neutrino flux agreed with the Solar Standard Model; however, they measured a non-zero flux for muon and tau neutrinos when the SSM only allows for electron flavor neutrinos. This is the first experimental evidence of neutrino oscillations. [9].

2.3 Atmospheric Neutrinos

Atmospheric neutrinos are the result of particle interactions in the atmosphere. Cosmic rays interact with the nuclei in the atmosphere to produce pions and kaons. The pions and kaons then decay into muons, electrons and neutrinos mainly governed by the processes

$$\pi^+ \rightarrow \mu^+ + \nu_\mu \tag{2}$$

followed by

$$\mu^+ \rightarrow e^+ + \nu_\mu^* + \nu_e \tag{3}$$

Super Kamiokande worked to find the ratio of muon-like events over electron-like events in their detector [7].

Downward going events, i.e. events that travel straight through the top of the detector, travel approximately 15km from the atmosphere before interacting in the detector. Upward going events travel through the earth from the atmosphere on the other side of the globe, approximately 13,000 km. A deficit in muon-like events was observed that was dependent on zenith angle while no asymmetry was discovered for the electron events. It was determined that this evidence of neutrino oscillations from muon-neutrino events turning into tau-neutrino events [7].

2.4 Neutrino Oscillations

Bruno Pontecorvo suggested a new theory of the neutrino in 1968 that would solve the solar neutrino problem. Up until 1968, the neutrino had been thought of as a massless particle. Pontecorvo put forth the idea that the neutrino oscillated flavor states (so in this case from electron flavor neutrinos to muon flavor neutrinos), a derivation will be given in a later section. In order for the oscillation to occur, the neutrinos must have a flavor mixing angle and distinct, non-zero masses [9].

Neutrinos have two sets of eigenstates; the mass eigenstates, and the flavor eigenstates. There are 3 flavor eigenstates, and they are electron flavor ν_e, muon flavor ν_μ, and tau flavor ν_τ. The flavor eigenstates can be thought of as a superposition of the mass eigenstates. The 3 mass eigenstates - denoted as ν_1, ν_2, and ν_3 - are most important during propagation of the neutrinos from the area of creation to the detector and are commonly treated as quantum mechanical plane waves. These two sets of eigenstates are related by the operator U, known as the Pontecorvo-Maki-Nakagawa-Sakata (PMNS) matrix, first introduced in 1962.

$$\begin{pmatrix} \nu_e \\ \nu_\mu \\ \nu_\tau \end{pmatrix} = U^\dagger \begin{pmatrix} \nu_1 \\ \nu_2 \\ \nu_3 \end{pmatrix} \tag{4}$$

There are many sources which derive the neutrino oscillation probability, the main one I used was [13]. In the formulation of neutrino oscillations, we will use the following assumptions to aid our derivation. First we will assume that the flavor eigenstates are a superposition of the mass eigenstates, mediated by some quantum mechanical operator.

$$|\nu_\alpha\rangle = \sum_k U^*_{\alpha k} |\nu_k\rangle \tag{5}$$

Second we will assume that the mass eigenstates, which we have defined as important during the propagation from creation to detection, can be expressed as plane waves which evolve using the Time Evolution Operator.

$$|\nu_k(t)\rangle = e^{-iE_k t}|\nu_k\rangle, \tag{6}$$

where E_k is the energy of the mass state. The oscillation will be controlled through a quantum mechanical operator $U_{\alpha k}$ that describes the superposition of the flavor eigenstates with the mass eigenstates, and we will see that this operator is in fact the rotation matrix for neutrino oscillations. From these equations we can now determine the complete time evolution of the flavor state by combining equations 5 and 6.

$$|\nu_\alpha(t)\rangle = \sum_k U^*_{\alpha k} e^{-iE_k t}|\nu_k\rangle \tag{7}$$

From equation 5 we can find $|\nu_k\rangle$ by multiplying on the left by $\sum_k U_{\alpha k}$. We also know that $\sum_k U_{\alpha k}U^*_{\alpha k} = 1$ because $U_{\alpha k}$ is unitary.

$$\sum_k U_{\alpha k}|\nu_\alpha\rangle = \sum_k U_{\alpha k}\sum_k U^*_{\alpha k}|\nu_k\rangle = |\nu_k\rangle$$

$$|\nu_k\rangle = \sum_k U_{\alpha k}|\nu_\alpha\rangle \tag{8}$$

When we combine equations 7 and 8, we find the original flavor state at the initial time is a superposition of different flavor eigenstates which we label as β. This equation gives us the transition from a pure flavor state at the initial time to a convoluted flavor state at a time greater than the initial time.

$$|\nu_\alpha(t)\rangle = \sum_\beta \Big(\sum_k U^*_{\alpha k} e^{-iE_k t}U_{\beta k}\Big)|\nu_\beta\rangle \tag{9}$$

We can find the amplitude of this oscillation of one flavor state to the other by multiplying equation 6 on the left by $\langle\nu_\beta|$. Orthonormality requires that $\langle\nu_\beta|\nu_\beta\rangle = 1$.

$$A_{\nu_\alpha\to\nu_\beta} = \langle\nu_\beta|\nu_\alpha(t)\rangle = \langle\nu_\beta|\sum_{\beta'}\Big(\sum_k U^*_{\alpha k} e^{-iE_k t}U_{\beta k}\Big)|\nu_{\beta'}\rangle$$

$$A_{\nu_\alpha\to\nu_\beta}(t) = \langle\nu_\beta|\nu_\alpha(t)\rangle = \sum_k U^*_{\alpha k} e^{-iE_k t}U_{\beta k} \tag{10}$$

If we take the modulus squared of the amplitude of oscillation found in equation 10, we will obtain the probability of oscillation. Equation 10 is time varying, thus we know that the probability of an oscillation will be time varying.

$$P_{\nu_\alpha\to\nu_\beta} = |A_{\nu_\alpha\to\nu_\beta}(t)|^2 = A_{\nu_\alpha\to\nu_\beta}(t)A^*_{\nu_\alpha\to\nu_\beta}(t) = \sum_k U^*_{\alpha k} e^{-iE_k t}U_{\beta k}\sum_j U_{\alpha j} e^{iE_j t}U^*_{\beta j}$$

$$P_{\nu_\alpha\to\nu_\beta} = \sum_k\sum_j U^*_{\alpha k}U_{\beta k}U_{\alpha j}U^*_{\beta j}e^{-i(E_k-E_j)t} \tag{11}$$

Now that we have determined the probability of an oscillation, we see that the probability is time dependent as predicted and is dependent upon the difference in energies between the two mass eigenstates. We can make an assumption, one that is used in typical neutrino oscillation derivations, that all detectable, massive neutrinos have the same momentum which we will define as p. We can assume this because the neutrino masses are much smaller than the neutrino energies during oscillation; thus, the energy equals the momentum to the first order. Changing the mass has no effect on the momentum for any given energy so we just set the momentum to p. We will also set c the speed of light equal to 1 and assume that the neutrinos have speeds comparable to c. We define $E = |p|$ as the relativistic energy of the neutrino in the massless approximation and using the binomial approximation, expand E_k.

$$E_k = \sqrt{p^2 + m_k^2} = E + \frac{m_k^2}{2E}$$
$$E_k - E_j = \frac{m_k^2 - m_j^2}{2E} = \frac{\Delta m_{kj}^2}{2E} \tag{12}$$

Now we can plug equation 12 back into the equation 11 for the probability as a function of time in parameters we can find.

$$P_{\nu_\alpha \to \nu_\beta} = \sum_k \sum_j U_{\alpha k}^* U_{\beta k} U_{\alpha j} U_{\beta j}^* \exp\left(-i \frac{\Delta m_{kj}^2}{2E} t \right) \tag{13}$$

Equation 13 is very useful, and we can consider ourselves finished at this point; however, the probability as a function of time is colloquially written as a function of the length that the neutrino travels. This is more indicative for experimental setup. In one of our approximations, we stated that the neutrino was ultra relativistic and thus the speed was very close to c. The time in the exponent can be written as $t = L/v$ where L is the length that the neutrino travels, and v is it's speed. If we approximate that $v = c$ then we can write $t = L$ in units where $c = 1$. We now have a general form of the probability of a two neutrino formulation oscillation.

$$P_{\nu_\alpha \to \nu_\beta} = \sum_k \sum_j U_{\alpha k}^* U_{\beta k} U_{\alpha j} U_{\beta j}^* \exp\left(-i \frac{\Delta m_{kj}^2}{2E} L \right) \tag{14}$$

This is the general form of the probability that a neutrino will oscillate from one flavor to another.

2.4.1 Two Neutrino Approximation

If we consider only 2 neutrinos as an approximation, we have one mixing angle θ and one difference in masses squared Δm. We can define our mixing matrix U as the rotation matrix.

$$U = \begin{pmatrix} \cos\theta & \sin\theta \\ -\sin\theta & \cos\theta \end{pmatrix} \tag{15}$$

Using Equations 14 and 15 we can find the probability in this two neutrino case.

$$P_{\nu_\alpha \to \nu_\beta}(L, E) = \sin^2 2\theta \sin^2\left(\frac{\Delta m^2 L}{4E}\right) = \sin^2 2\theta \sin^2\left(1.27\frac{\Delta m^2[eV]L[km]}{E[GeV]}\right) \tag{16}$$

Where the constant 1.27 comes from the change from SI units to the units of eV for mass, km for length, and GeV for Energy.

2.4.2 Full Three Flavor Mixing

In the full three-flavor formalism, the matrix U is a 3×3 rotation matrix. It is useful to factorize the rotation matrix into 3 terms:

$$U = \begin{pmatrix} 1 & 0 & 0 \\ 0 & \cos\theta_{23} & \sin\theta_{23} \\ 0 & -\sin\theta_{23} & \cos\theta_{23} \end{pmatrix} \begin{pmatrix} \cos\theta_{13} & 0 & \sin\theta_{13}e^{-i\delta} \\ 0 & 1 & 0 \\ -\sin\theta_{13}e^{i\delta} & 0 & \cos\theta_{13} \end{pmatrix} \begin{pmatrix} \cos\theta_{12} & \sin\theta_{12} & 0 \\ -\sin\theta_{12} & \cos\theta_{12} & 0 \\ 0 & 0 & 1 \end{pmatrix} \tag{17}$$

The PMNS matrix can be factorized such that each matrix has only elements of a specific mixing angle known as θ_{23}, θ_{13}, and θ_{12}, meaning each matrix describes a mixing between two states. Historically, neutrino oscillation theory is built on a two flavor mixing formulation as we saw from our two flavor approximation calculation. It is useful to think about the the PMNS matrix as a rotation matrix that has been extended to a third dimension.

To understand why the PMNS matrix is factorized this way, we must look at the typical oscillation length as given by equation 16. We look at the component of the probability $\sin^2(1.27\frac{\Delta m^2_{jk} L}{E})$.

Solving for L to find the oscillation length we see that

$$L_{oscillation} = \frac{\pi E}{1.27\Delta m^2_{jk}} \tag{18}$$

Thus the length that the neutrino travels is constrained. Note that L must be close to $L_{oscillation}$ or else there will be no oscillations. If $L >> L_{oscillation}$, then the oscillations will be averaged out; if $L << L_{oscillation}$ there will be no oscillations. Therefore, experiments are determined by the level of sensitivity of Δm^2_{jk} and thus determined by L and E [14].

The θ_{23} sector is associated with atmospheric neutrino data with a mass squared difference known as Δm_{23}. Cosmic radiation is constantly raining down upon the earth. Neutrinos are constantly flowing through the Earth. As the radiation enters the upper atmosphere, a large amount of pions are created. These pions decay into muons and muon neutrinos that then cascade down onto and through the earth. Atmospheric experiments have a length anywhere between 20-10000km and an energy range of 0.5-100GeV, thus their Δm^2_{jk} sensitivity is approximately $10^{-3}eV^2$ [14].

The angle θ_{12} is associated with solar neutrino data. The sun is fueled by proton-proton reaction chains that turn Hydrogen into Helium modeled by:

$$^1_1H +^1_1 H \rightarrow^2_1 H + e^+ + \nu$$
$$^2_1H +^1_1 H \rightarrow^3_2 He + \gamma$$
$$^3_2He +^3_2 He \rightarrow^4_2 He +^1_1 H +^1_1 H$$

A low energy neutrino is released in this process and the length from creation to the detector is extremely long. This causes solar neutrino experiments to be sensitive to very low values of Δm^2 approximately 10^{-5} [14].

The last section of the PMNS matrix is often called the "cross-mixing" matrix. The mixing angle θ_{13} measures the portion of ν_e that is a part of ν_3. Everything discussed so far is known and has been measured to a particular degree of accuracy, except for the one piece of the cross-mixing matrix. The phase violating factor δ_{CP} is still unknown. With the development of higher precision long baseline neutrino experiments, and the discovery of a nonzero θ_{13}, the three matrices can be exploited to further investigate the phase violating factor δ_{CP}.

To find δ_{CP}, experiments observe ν_e appearance in a ν_μ beam. The probability of this oscillation is given by

$$P_{\nu_\mu \to \nu_e} = \left| \sqrt{P_{atm}} e^{-i(\frac{\Delta m^2_{32} L}{4E} + \delta)} + \sqrt{P_{sol}} \right|^2, \tag{19}$$

where $\sqrt{P_{atm}}$ and $\sqrt{P_{sol}}$ are the two flavor oscillation amplitudes of the atmospheric and solar sectors [22]. Many of these parameters are known, thus we can analyze the probability of the oscillation for neutrino and anti neutrino events. It is known that δ_{CP} changes sign between neutrinos and antineutrinos, so we look for the difference between the two and single out δ_{CP} [19].

It is from this point forward that neutrinos have become the focus of intense study in high energy physics research: studying the non-zero masses of neutrinos and their oscillations, studying the mixing angles of neutrino oscillations, determining the neutrino mass hierarchy, finding more accurate values of δ_{CP}, and much more.

Many experiments, current and proposed, are designed to study neutrino oscillations. Such experiments include MINOS, CHIPS, NOvA, T2K, Super-Kamiokande, Hyper-Kamiokande, SNO, LBNE, etc. This proliferation of experiments within the past 50 years shows that the study of neutrino physics has a future and that there is still much more work to be done.

2.5 Detector Technology

To measure ν_e appearance, we need a detector with good electron identification. In order to accomplish this, the detector must be very massive in order for the charged particles to interact in the detector. Next generation experiments strive for masses on the order of 100ktons. Water cherenkov detectors are a proven technology that meet both of these requirements. Water cherenkov detectors utilize cherenkov radiation in order to visualize particle interactions inside the detector volume.

The speed of light in a medium is proportional to the ratio of the speed of light c to the refractive index of that medium. The velocity of light is 25% slower in water than in a vacuum. In water cherenkov experiments, neutrinos interact with the nucleons in the water to create charged particles which are traveling faster than the velocity of light in water. The charged particles have an associated electric field with them which is carried by photons traveling at the velocity of light

in water; thus, the propagating photons carrying the electric field do not interfere with one another. This causes a "photonic boom" similar to that of a sonic shock wave. As this wake travels through the medium, it excites the electrons in the atoms, as they de-excite they emit photons of frequencies in the range of blue visible light to UV light [11].

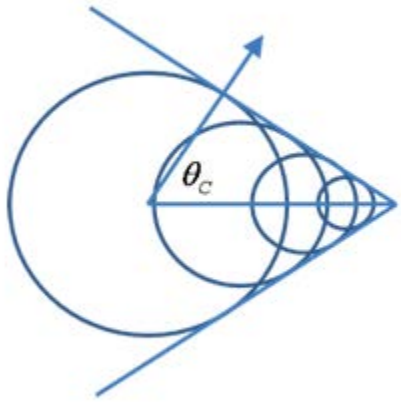

Figure 1: A graphical depiction of Cherenkov radiation as a charged particle moves through a medium.

These photons are emitted in the shape of a thin, conical shell whose central axis is along the charged particle's path. This cone radiates outward with a solid angle θ_c which is inversely proportional to the medium's index of refraction [12]. Photo Multiplier Tubes (PMTs) can detect these Cherenkov photons. An event display shows the charge of the PMTs activated during an event, and the time distribution of the hits in those PMTs. With this event display, the cone is visualized as a two dimensional ring on the wall of the detector.

When a neutrino enters the water of the detector it has two options to interact. There are charged current interactions in which the neutrino is transformed into its charged lepton counterpart, or neutral current interactions where the neutrino scatters off of a particle or breaks a molecule up into its constituent parts. Charged current interactions are easier to work with in detectors because we can then identify the flavor type of the neutrino based off of the emitted particle. Neutral current events transfer momentum to the particle that it scatters off of, which we can then detect if the momentum is high enough that the particle emits Cherenkov Radiation [18].

Water Cherenkov detectors find ν_e events with an accuracy of 80% with the ν_e charged current events having a single Cherenkov ring and the neutral events having two Cherenkov rings that overlap [21].

So now we know how cherenkov radiation works, how do we find electrons in a water cherenkov detector versus another charged particle such as the muon? When an electron is in the vicinity of a nucleus or an ion, it can do many things to interact with that nucleus. One interaction, Bremsstrahlung, or braking radiation, is characterized as follows: as the electron passes near the ion, it can decelerate resulting in a loss of kinetic energy. In order to conserve energy, a photon must be radiated.

As the charged particle decelerates, its power can be approximated by the relativistic Liénards generalization of the Larmor formula :

$$P = \frac{\mu_0 q^2 \gamma^6}{6\pi c}(a^2 - |\frac{\mathbf{v} \times \mathbf{a}}{c}|^2) \tag{20}$$

where $\gamma = 1/\sqrt{1 - v^2/c^2}$. We know that the relativistic energy of the particle will be $E = \gamma mc$. Thus γ is proportional to $1/m$. We then can come to the conclusion that the power radiated goes as $1/m^6$. Thus more massive particles such as the muon do not experience Bremsstrahlung at GeV energies.

When a photon interacts with a nucleus, a charged particle and its anti-particle can be formed in the process known as pair-production. The photon interaction must have enough energy to equal the rest mass of the pair in order for creation to occur. With an electron-positron pair, these two particles can then go through the process of Bremsstrahlung again and create more photons which will then interact. This process is known as an electromagnetic shower. At the high energies, the electron will experience Bremsstrahlung and pair production until the photons emitted during Bremsstrahlung are below the rest mass threshold. This shower of particles in the detector creates a fuzzy cherenkov cone. The muons do not experience Bremsstrahlung, thus when a muon interacts in the water cherenkov detector, there is a sharp ring. We can utilize this phenomenon to identify electron versus muon interactions in the detector.

3 Building the Detector

3.1 Instrumentation

CHIPS-M is a water Cherenkov Detector, thus it looks at the Cherenkov light emitted in water as charged particles pass through the medium. To study these effects, CHIPS-M is instrumented with five 13" Hamamatsu DOMs (Digital Optical Modules) from the IceCube neutrino project. A DOM is a large glass sphere with a main board computer in the top hemisphere and a PMT in the bottom hemisphere. Each DOM has a pigtail which runs from the top of the DOM to the outside of the detector where it connects to a cable. This cable runs from the detector to the DOMhub computer where it can then transfer data to and from the detector.

The DOM's PMTs use the photoelectric effect to collect data. An incoming photon from Cherenkov Radiation in the detector will knock off an electron from the cathode. This electron then travels down a dynode chain in which the initial electron from the cathode knocks off more from the first dynode. This causes a cascade of electrons as they travel down the chain to the anode where a large current is read out. The data we read out from these PMTs is in photoelectrons (p.e.) which is how many electrons were liberated at the cathode. The DOM main board starts taking data when the charge read out from the DOM is above a specific threshold, 2 p.e. in our case [23]. We can then find data such as the time of each hit, the charge, and the time it took to integrate half of the charge.

3.2 Skeleton and Liner

The construction of CHIPS-M began at the College of William and Mary in May 2014. I began the construction of two large octagonal pieces of aluminum truss that would serve as the top and bottom of the detector. This truss structure is commonly used in concerts as the support for the sound equipment, meaning it is portable and extremely light. The octagonal tops and bottoms were approximately 3.5 meters long when fully constructed. The legs that would attach the top and bottom together were 10 foot stainless steel beams to prevent any corrosion inside of our detector. Will Henninger - the College of William and Mary machine foreman - and I machined the rest of the parts for the CHIPS-M structure using the Computer Numerical Control (CNC) machine and shipped them to Soudan, Minnesota where construction would continue.

Figure 2: Kora Caramitsos (left) and me (right) posing next to one completed truss structure.

Our first task when the detector arrived at the MINOS Surface building in Soudan, Minnesota was to attach a water and light tight liner to the top and bottom of the octagonal truss sections. The liner was to ensure that the purified water inside the detector would not leak out. We also wanted to prevent any light leaks from interfering with out experiment since we are sensitive to excess photons. We layered a special liner tape and the liner against a special bar attached to the aluminum truss and then clamped the liner down with an additional aluminum bar and bolts. This method of clamping with a layer of tape proved to be light tight when we tested the detector before deployment.

The clamping seemed to work during the initial stages of the detector when it was above water. Current data shows that we might have a water leak and a light leak inside the detector. This process will have to be reevaluated in a lessons learned when we pull the detector up during the summer of 2015. Some students worked on other ways of sealing the liner, such as a weld in which extreme heat is applied to fuse the two pieces of liner together. This process was difficult to perform, but was resistant to pulling the pieces apart. More tests will have to be performed to ensure the stability of the weld to light tightness and water tightness.

We then began constructing the skeleton of the detector. Using a large shop crane we flipped the bottom octagonal piece so that we could attach the legs. After bolting the legs to the bottom truss, we then lifted the top octagonal truss piece to bolt it to the top. It is imperative to ensure that the DOMs are facing upstream towards the beam from FNAL, thus torsional movement has to be limited. To prevent this movement, we attached support wires along the diagonals of the detector. These wires were tensioned such that the detector's shape would not distort when it was picked up with a crane. The side liner was added at the very end of construction using an identical sealing process as for the end caps with a large vertical bar attached to one side to clamp the liner.

Figure 3: The detector after installation of the diagonal support wires.

3.3 DOM Cables

I travelled to Madison, WI to work on 5 spools of 1000 ft cable that would relay information from our detector in the water to the domhub back on shore. The 1000 ft of cable needed a splice that is water-proof to connect a XSJJ DOM connector to the cable. I worked with Andrew Laundrie of the IceCube project to develop a splicing technique that would prove to be waterproof. I also

wrote a manual documenting the entire process for future reference (see Appendix A). I drove back to Soudan, MN on July 5, 2014 to continue working on the construction of CHIPS-M.

3.4 Mirrors

It was suggested that we should install two mirrored surfaces inside of our detector in order to aid in the veto of the 150 Hz frequency of cosmic muon events. These mirrors would help in the interception of the cherenkov radiation from the cosmic events that would enter from the top of the detector. We can then measure the time difference between the hits and determine if they were delayed from the reflection. The mirrors are 100 cm squares of Lexan coated in a mirrored surface. The original mirrors were Lexan squares coated in ReflecTech; however, RefelcTech is a self adhesive. The self adhesive proved not to be as effective because it formed bubbles of air below the mirror which would distort our measurements.

3.5 DOM Installation

The DOMs are supported by square mounts developed by the physicists at the University of Texas. These mounts are built to support the 12.7 kg mass of the DOMs and are angled by the use of floats while there is water present in the detector. This angling was found to maximize the collection of cherenkov light emitted by NuMI beam muons in the water. After installation, we covered each DOM in order to prevent the degradation of the cathode from the environmental UV rays and harsh shop lights. Once we were prepared to install the side liner on the detector, we removed the covers.

Four DOMs were installed on the side facing the NuMI beam line from Chicago near the top of the detector. One DOM was assigned to be the veto DOM which was placed on the side opposite of the beam line DOMs. This veto DOM was attached approximately near the bottom of the detector in front of the two mirrors. During deployment, the veto DOM became detached and floated to the surface of the detector. We are unsure as to the reason of this happening, but the DOM has been rendered useless. We are currently taking data with four fully functional DOMs which has proven enough to study the cosmic ray rate.

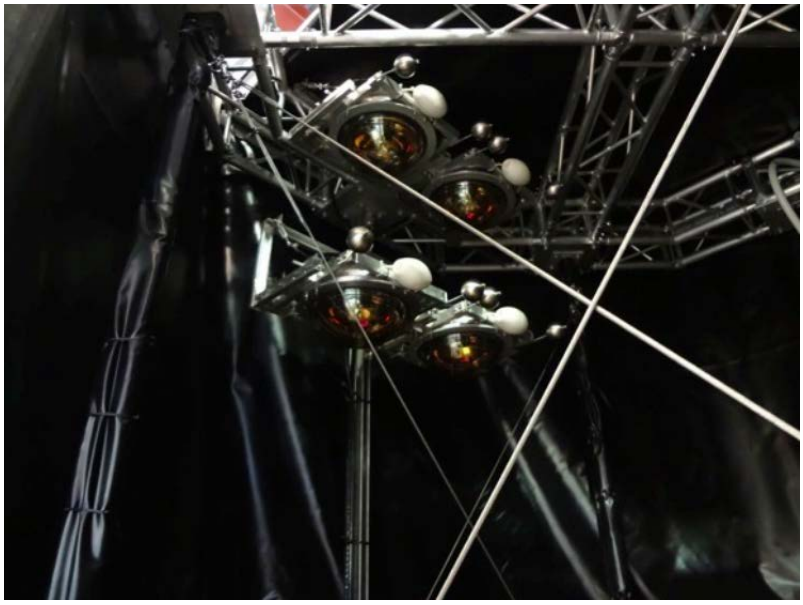

Figure 4: 4 of the DOMs in the CHIPS-M module detector

3.6 Plumbing and Filtration

The water of the Wentworth Mine Pit is remarkably clear for a lake. At wavelengths of 300-500nm, the attenuation is approximately 1-5 m. However, our detector is approximately 3.5 m, so we are losing $\frac{1}{e}$ amount of photons within our detector length. We need an even better attenuation length than that, especially in the future larger detectors. One way to do this is to filter the water through our pump constantly. The CHIPS-M module has two hoses coming out of the detector and leading back to shore. One hose was used to initially fill the detector with water during the deployment process. This hose is then reused along with the second hose to recirculate water from the detector, through the pump and filters, then back out to the detector. One hose is a 1" diameter white spa hose, and the other a 3/4" diameter white spa hose. The 1" spa hose is used for the initial fill process and then is used to pump water through the filters. To prevent a manual changing of hoses for this process, I developed a filling and recirculation scheme in which ball and T valves are used to divert the water (see Appendix B). During the filling process with approximately 100 ft. of hose, we can achieve a flow rate of 15 gal/min. With a calculated 9000 gal of water, we can expect a 10 hour fill time.

One of the goals of CHIPS-M is to see how large of an attenuation length we can achieve

with this prototype. We are using many particulate filters ranging to 0.22 μm and a UV sterilizer. Currently, data is being tested at the university in Duluth. We have achieved a better attenuation length, but black sludge has hampered further improvements.

3.7 Deployment

On the morning of July 29, 2014, the detector was loaded onto a large trailer to begin its journey to its resting place. The detector was driven along the highway 25 miles from the construction MINOS surface building to the Wentworth mine pit. The speed of the trailer never exceeded 30 mph to ensure minimal DOM vibration. The detector arrived safely to the mine pit without any hitches in the plan. When the detector arrived, it was craned off of the trailer and onto the legs that were assembled in the surface building. The legs supported the detector so that it does not have to sit at the bottom of the lake on the ground.

To ensure the safety of the cables traveling from the detector to the shore shed, an "umbilical cord" was created to house the cables and plumbing. To create this umbilical cord, extremely long lengths (approximately 800 ft) of corrugated tubing was cut. The tubing was really durable and hard to bend so we created a tool called the longhorn which spreads the tubing apart and inserts the cables as you pull it down the corrugation. This tool cut the time of creating the umbilical cord from several days to a few hours. While a crew was working on the umbilical, a separate crew began working on the floats that would attach to the top of the detector.

Figure 5: The "long horn" built as a tool to insert cables into the corrugated tubing.

The Large Lakes support-team decided that floats attached to the top of the detector would prove easier to tug the detector out into position once it was deployed onto the lake. A crew of us helped attach these floats by climbing up a ladder and securing the floats to the crane handles on the detector. This would allow easy access for the crane to attach to the top of the detector, and easy detachment of the floats once the detector was in the water.

The detector was deployed into the water on July 31, 2014 at the Wentworth Mine Pit. While the detector was lowered into the water, filtered lake water was slowly pumped into the detector. The total filling process took approximately 10.5 hours to complete. The detector submerged up to the attached floats at the end of the day on the 31st. The Large Lakes crew came back the next day August 1, 2015 to tow the detector out to its resting place and detach the floats. The detector sank slowly to its final resting place at the bottom of the lake and rests there now with less than a degree of variance in its angle of tilt due to readings from a monitor in the outside of the detector.

Figure 6: The last night of CHIPS-M on land in the sunset

4 Operations

The first few runs of data taken during the first day after deployment showed very anomalous behavior. The DOMs were completely saturated by outside light sources. It was apparent that there was a light leak in the detector, forcing the collaboration to start taking data solely during the night. We hoped that during the winter, the surface snow accumulation would allow us to take data throughout the day, but that was not the case. There was snow accumulation on the top of the lake, but it was not substantial enough to prevent any incoming light from affecting our data. We take data in intervals called runs, where each run is 58 min long starting at 9pm in the evening. We take continuous runs until 6am the next morning (adjustments for daylight savings time are taken into account). The DOMhub computer reads in all of the data from the DOMs and writes an output text file which is then transferred over to FNAL.

During the winter, the lake froze over on top and snow piled up creating a substantial shield to the outside light, but it was not substantial enough to start taking data during the day. Each DOM has LED flashers that help us take data by sending out an LED pulse that is built into the

DOM. From this pulse we can sample the light level in the detector from a known source of a known magnitude. One problem that was observed using the LED flasher was a drop in light level.

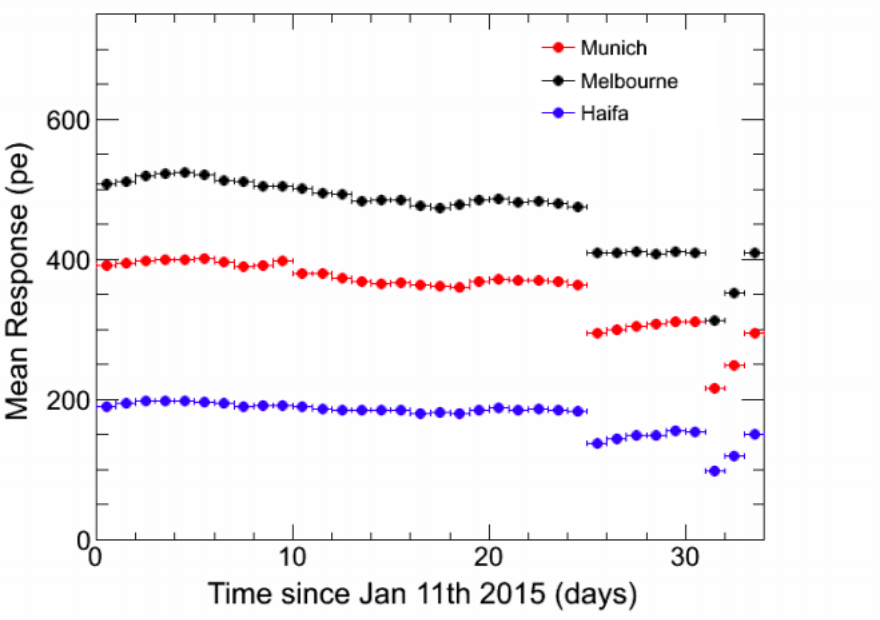

Figure 7: A Plot of a drop in the light level in our detector

The drop in light level was believed to be a thick black sludge that clogged our filters in the pump. In this plot you can see two noticeable drops in the light level [3].

4.1 Bacteria and Black Sludge

During data collection we noticed a "black grime" in the filters of the pump. It was hypothesized that this was possible corrosion of the liner material. I had a hypothesis that predicted sulfate reducing bacteria to be the cause. My hypothesis stated that the black sludge in the 5 micron water filters is insoluble Iron II Ferrous Sulfides resulting from a reaction of hydrogen sulfide and metal particles in the Wentworth Mine Pit Water.

The Wentworth Mine Pit surface water is high in sulfates. The specific concentration is listed as 120 $\pm$ 25 mg/L [20]. Common listed sulfate concentrations of mine pit waters in Minnesota are 100 - 1500 mg/L levels [2]. With these higher levels of sulfates come the introduction of Sulfate-Reducing Bacteria (SRB) which are commonly used to treat high concentrations of sulfates in mine water. Typical metals such as carbon steel or iron corrode by the following process: when water

hits the metal, a layer of molecular hydrogen is formed over the surface of the metal. SRB create energy under low oxygen conditions by oxidizing the molecular hydrogen creating hydrogen sulfide as a waste product [25]. The hydrogen sulfide reacts with the metal ions in the pit water and produce metal sulfides. These metal sulfides are insoluble, thus they will show up in the CHIPS-M filters [10]. One common metal sulfide example is Iron (II) sulfide or Ferrous Sulfide which is black or dark brown in color.

Stainless steel is a steel alloy (content includes iron, chromium, manganese, silicon, carbon and significant amounts of nickel) that has a minimum of 10.5 percent chromium content [24]. The high chromium content is important in its anticorrosive properties. When water hits stainless steel it still forms this layer of molecular hydrogen and other corrosive products. The difference is that a layer of chromium oxide, formed from the interaction of the high chromium content and oxygen, coats the steel beneath this surface of corrosive material to prevent further corrosion [26]. The important part is that the hydroxides are still present without the further corrosion of the metal. The Wentworth Mine pit does have an iron content of <50 μ g/L [20], so the Ferrous Sulfides can be formed by this process in the detector. Further chemical analysis of the "black sludge" has confirmed that the sludge is zinc sulfate which supports my hypothesis, only the likely cause of the sludge is the zinc currently in the water.

The black sludge has so far hampered our improvements in the attenuation length and also effected our data. We have seen light drops when the black sludge is most prevalent in the filters and we have many runs where we see a significant and sudden drop in the cosmic ray rate. On February 5th is when the first light level plummets and February 11th is the next day.

5 Data Analysis

The data from the DOMs in the detector is written to .txt files on the DOMhub main computer. The files are then transferred to disk space at Fermilab National Accelerator Laboratory where I can then access them from my personal computer. Each row in the text file is one PMT hit. Each hit consists of a charge, time stamp, the name of the PMT hit, and a timing offset of interpolation of 50% of the charge. I had to write an analysis code that clusters these hits into events. CkovHit reads in the raw data text files and stores the data in a different format. The

CkovEvent class then groups these events based off of time windows between hits. CkovEventSum looks at the events in each run file and stores overarching data related to that run. These classes are linked in a shared library that links with the various ROOT libraries needed for analysis. For a detailed description of the variables used in the code, see Appendix C. I also created a pseudo Event Display that gives a visual representation of the event inside the detector related to the time distribution of each hit in the event and the size of the charge of each hit.

5.1 Raw Hit Data

Our raw hit data is in .txt format on the DOMhub computer. We must manually transfer those files over to the Fermilab computing space that is allocated to chips and from there we can interpret the data. I created a macro called CkovHitTree that creates a root file of all of the raw data. From here we can then study the data of the individual hits in the detector and the DOM sensitivity to the apparent light leak.

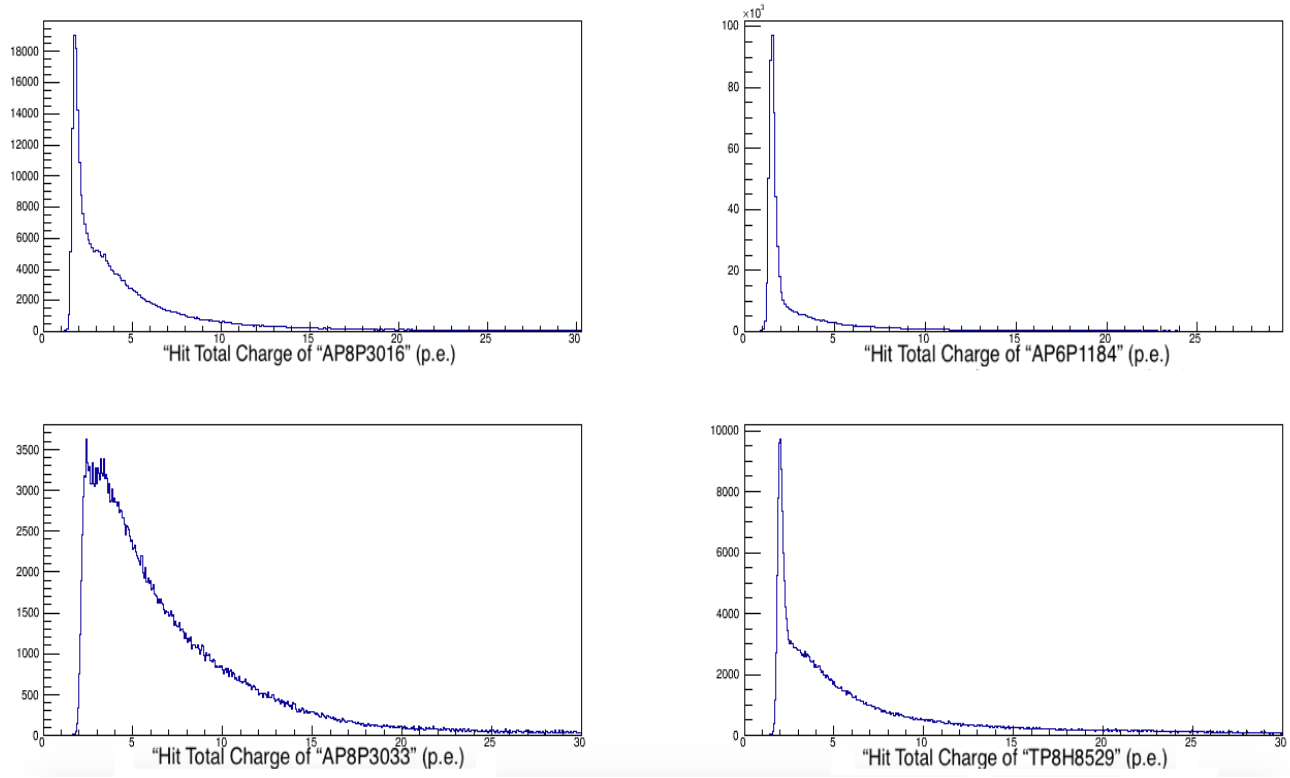

Figure 8: Total charge (p.e.) integrated in the detector from runs 0009 - 0099 with cuts based on domID (name of the DOM in the DOMhub DAQ code).

All of the DOMs in Figure 8 seem to be behaving as expected; however, we see in DOM AP8P3033 that there is a different structure. This is believed to be due to the higher cutoff of the charge in that PMT. We had seen before that this DOM was very noisy while on shore, thus a higher cutoff rate was applied to reduce the noise in this DOM resulting in the limited shape. DOM AP6P1184 is also very noisy, but this DOM did not receive a cut. The DOMs TP8H8529 and AP8P3016 are all approximately at the same level which is consistent with what we want.

5.2 Event Data

From the HitData I began to think about how to group the hits into what is known as an event in high energy physics. In an event, a single interaction will cause a number of DOMs to fire due to the Cherenkov radiation in the detector. Since many DOMs may fire in a short time span, we can assume that these DOMs fired due to the same charged particle. The difficult part is finding how short or long to make the time span in order to not group unrelated hits together, and also not leave any hits out of the grouping. To do this, I created a macro called CkovEventTree which groups the events and studies the total charge of the event, and the time width of the event.

A difficulty arose when designing this macro and I was organizing the hits in time order. Each hit is given a GPS time stamp from the DOM when it is recorded in its raw form. We define the hit time as the time stamp given to the charge plus the time it takes to integrate half of the charge in the DOM (defined as t50 in the raw data). T50 is not the same for every hit, and some hits could take longer to integrate than those that come after it, so the hit time order is not the same as the GPS time stamp order. My solution was to use a multi map to sort the data by hit time which is GPS time plus t50 time. Once I successfully solved this problem, we proceeded with the analysis.

We thought it might be interesting to group hits into events based off of gaps in the timing distribution. After looking into the documentation for the DOMs and the timing characteristics of the electronics, it was apparent that this was not going to be possible. There is a large delay after each hit is processed in the DOM that there will always be noticeable gap. Starting with the first hit in the HitTree, we decided to group the events within a specified time window. I created event groupings in time windows of 5, 7, 10, 12, 15, 20, and 50 ns.

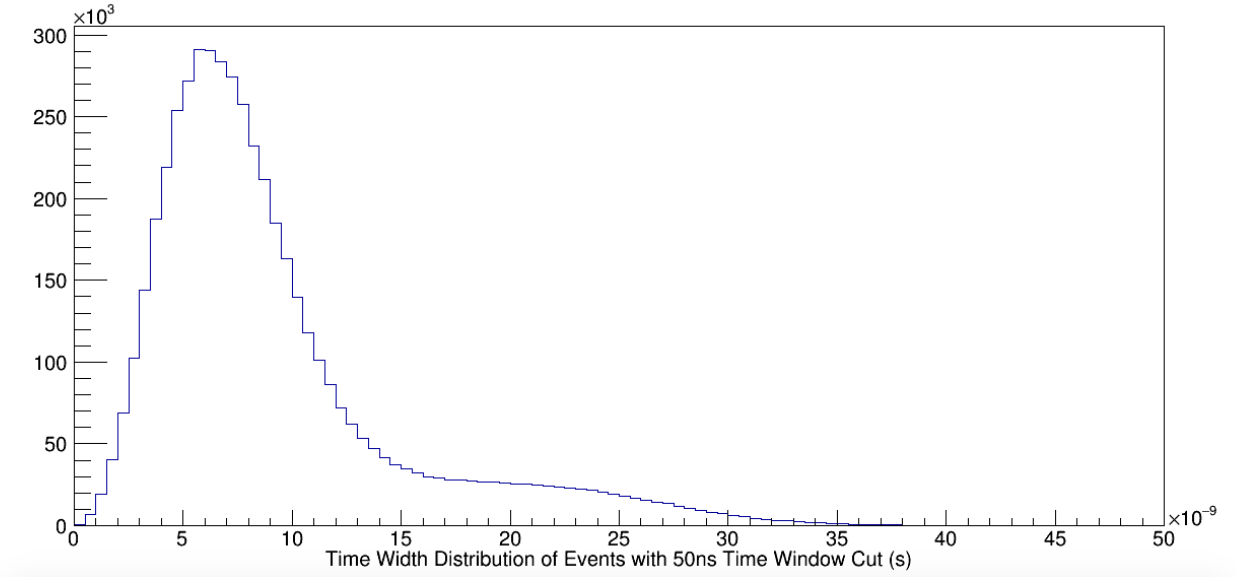

Figure 9: The time width of the events distribution, 50 ns time window with 4 hit coincidence.

Figure 9 was created using a 50s time window with a 4 hit coincidence cut. As you can see, there is a distinct bump centered around 8ns that most of the hits fall into. There is also a significant shoulder that begins around 15ns. It is obvious that the 5ns time window is not inclusive of everything that we expected to see. The window cuts off most of the distribution. The mean of the distribution is approximately 6 ns, but that is also too short of a time window to justify the cut. We must find a time window that will eliminate any accidental grouping of singles into larger events and yet not be too short to cut off any of the distribution.

The time window was cut prematurely for all of the time windows until the 15 ns time window. Following the 15 ns time window we start to see the beginnings of a second bump at a later time in which there seems to be a surge of events happening following the initial events. In Figure 10, the 50 ns time window, there is a secondary bump. This bump is the same as in Figure 9 and is hypothesized to be the accidental grouping of extraneous single events being grouped incorrectly into larger events. In my code I check to see if the same PMT is firing in one event, an effect known as afterpulsing. Afterpulsing effects occur when the electron that initially impinges on the cathode breaks off ions which then impact the cathode and release more electrons.

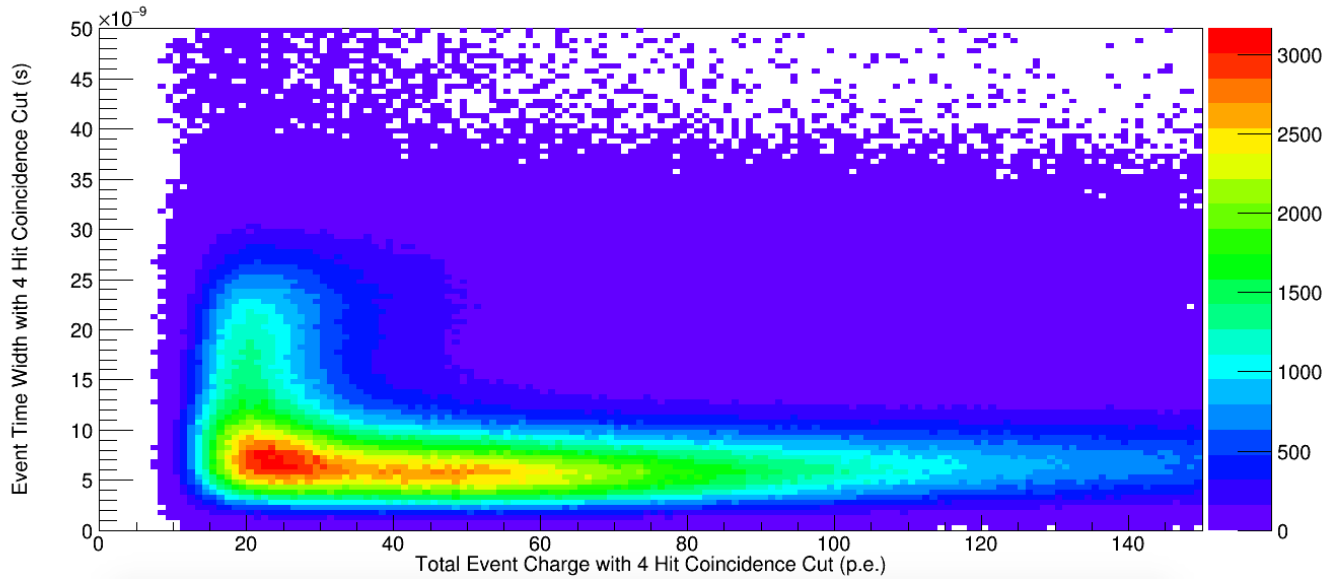

Figure 10: Total charge (p.e.) integrated over the event versus the time width of the event under a 50 ns time window and 4 hit coincidence.

In Figure 10, we notice that at higher time widths, we are only grouping smaller charges explaining the vertical green band centered around 20 p.e. Since we are only grouping four single hit charges, which tend to be small, the overall charge of the event will also be small. This is why the vertical band is very narrow (approximately 20 p.e.). At approximately 15 ns and below, we are grouping events with large charges indicative of the colorful band at low time widths. These large charges lend themselves to cosmic ray interactions versus the smaller charges which we surmise to be accidental single hit groupings. From this event rate data we see that 15 ns seems to be a very attractive time window from which to group our hits. We investigate this further when we look at the summary data for the event runs.

5.3 Event Rate Data

I next took all of the event data and created a summary tree for each file using a macro called CkovEventTreeSummary. This tree holds data such as the rate of single coincidence, double coincidence, triple coincidence, and quadruple coincidence events as well as the total time of the file (approximately 58 min for each run). This tree is will hold data such as the moon rise and set time, along with sunrise and set times.

I first plotted the rate of hits as a function of the run number.

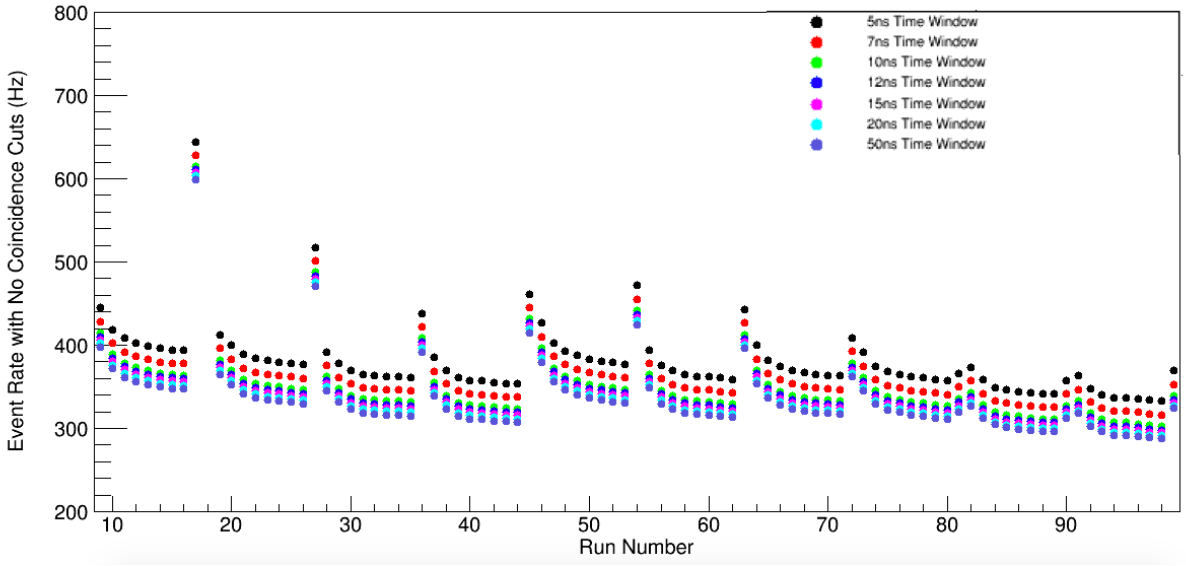

Figure 11: The Total Event Rate vs. Run Number for runs 0009-0099.

As you can see in Figure 11, there are instances in the runs where the event rate spikes. We can understand this as part of the light leak saturation of the DOMs. At the beginning of data collection, some of the runs ran over into the daytime and due to the light leak, the DOM data was saturated. We eventually solved this issue but the constant battle between the change of sunrise and sunset proved to be difficult. We also suspect that the High Voltage Supply of the DOMs was still warming up during this time.

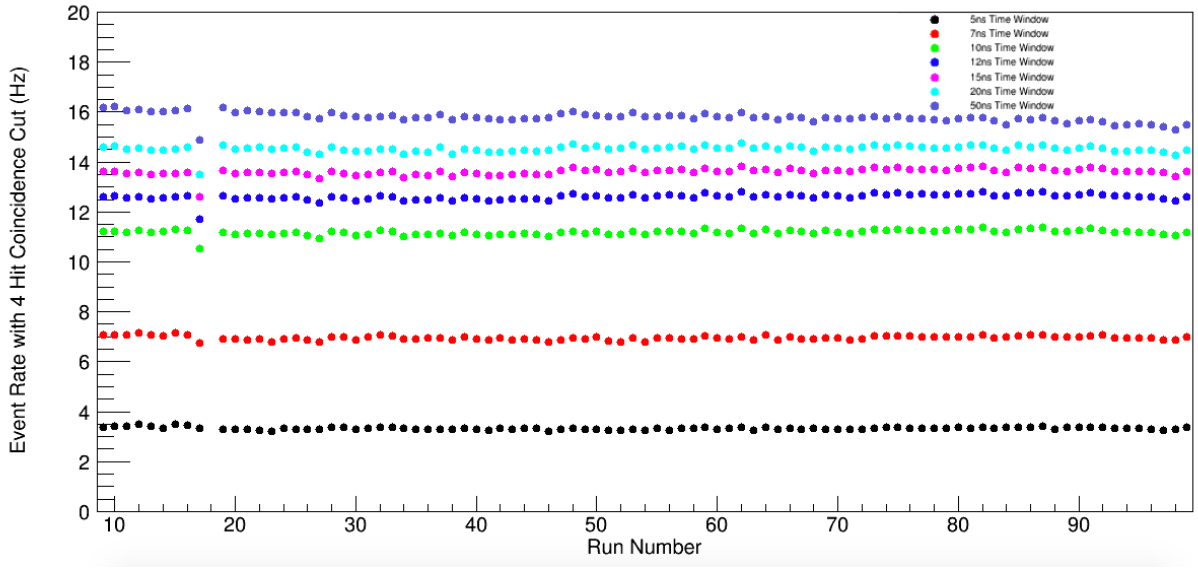

Figure 12: 4 Coincidence Event Rate All Time Windows vs. Run Number for runs 0009-0099.

In Figure 12, as the time window gets larger there is an increase in the rate of events for four coincidences. This is obvious in that as the event window gets larger, more hits are probable to be grouped into these events. This plot differs from the total hit event rate because as we limit to 4 hit coincidences, we eliminate a lot of the noise from the light leak and PMT noise.

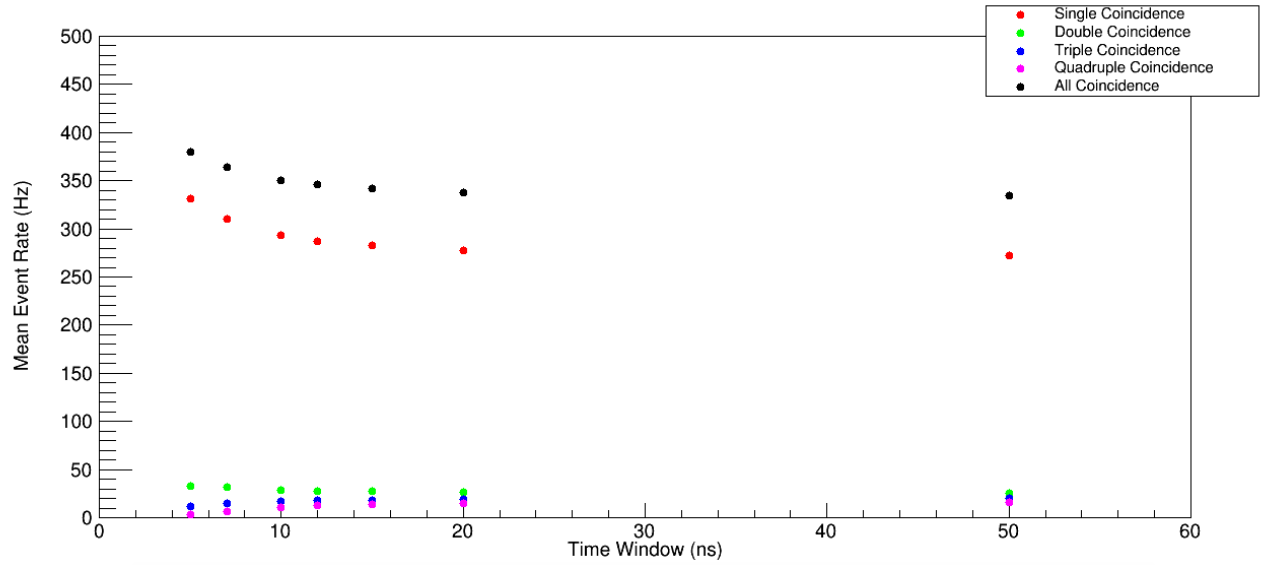

Figure 13: Event Rate versus the Event Time Window for runs 0009-0099.

In Figure 13, we confirm that as the time window increases the triple, and quadruple coincidence event rate increases. This corresponds to a similar decrease in the rate of the double, single and total hits. In Figure 13, at approximately 15 ns, there is a leveling off of the event rate in all coincidences. This observation leads us to conclude that 15 ns is an appropriate event rate time window. With this time window we can be sure that we will capture real physics events in our detector while minimizing the background noise from single events. We proceeded with our analysis of the environmental effects on the event rate using this time window.

In order to check our rates, we will derive the frequency for the number of interactions in our detector using [17]. We can use the same model as the frequency function for number of nuclear decays. We first assume that the one interaction in our detector is completely random. Thus the probability for an interaction in our detector in a specific time interval Δt is proportional to the interval and mediated by some proportionality constant of inverse time.

$$p = \lambda \Delta t \tag{21}$$

Since we are taking a larger sample of N interactions, we can say that the probability of 1 interaction out of all of the N interactions in a time Δt is given by

$$P = \lambda N \Delta t \tag{22}$$

This looks similar to the origins of a Poisson distribution. Thus the probability for obtaining n decays in a time interval Δt is given by the Poisson distribution function.

$$P(n,t) = \frac{e^{-\lambda N t}(N\lambda N t)^n}{n!} \tag{23}$$

Thus the average number of interactions is give by the first moment of this Poisson distribution which is $\overline{n} = \lambda N t$. If we investigate large samples, we know that the total sample will decrease by an amount ΔN.

$$-\Delta N = N\lambda \Delta t \tag{24}$$

Making equation 24 a continuous function, we find

$$\frac{dN}{N} = -\lambda dt \tag{25}$$

Solving this differential equation for N

$$N(t) = N_0 e^{-\lambda t} \tag{26}$$

I calculated the time difference between the different coincidence events and using an exponential fit, found the time constant for these events as seen in Figure 14. This time constant is the rate at which these events occur.

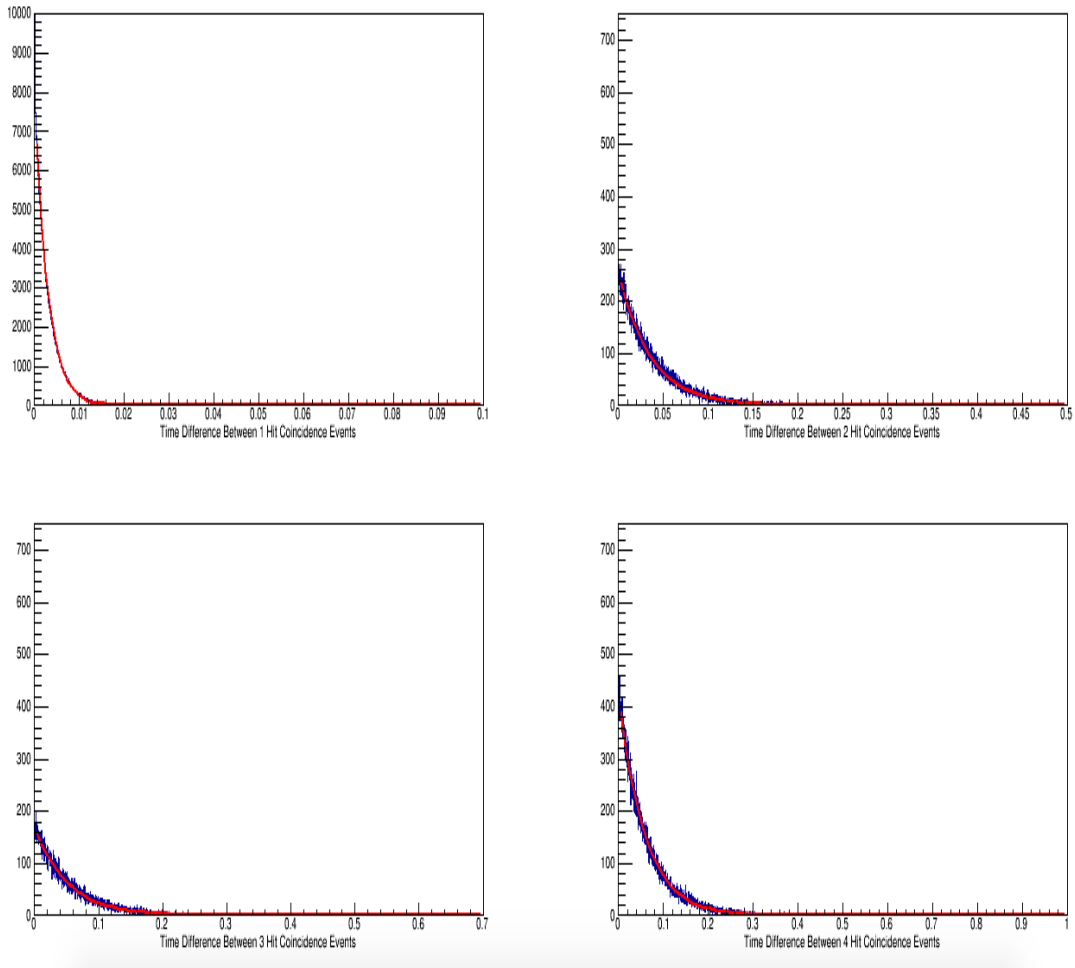

Figure 14: An exponential regression check on the event rates for run 0009.

Table 1: Exponential Regression Check

	4 Hit Rate	3 Hit Rate	2 Hit Rate	1 Hit Rate
Analysis	13.5Hz	18.5Hz	27.9Hz	346Hz
Exponential Fit	17.1Hz	19.2Hz	27.7Hz	337.9Hz

Table 1 shows that the rates from my analysis match up well with the expected rates of a random distribution of interactions in our detector from exponential regression.

5.3.1 Environmental Effects on the Event Rate

The outside environment will have a major effect on the detector, and the better we understand this environmental background effect on the cosmic ray rate, the better prepared we will be when the larger phases of the CHIPS project will be constructed and deployed. One effect we can look at is what we can see now that we have a light leak in our detector. We should be able to see certain effects from the environment such as the moon phases and their eventual decline due to the snowy cap that eventually falls on the mine pit.

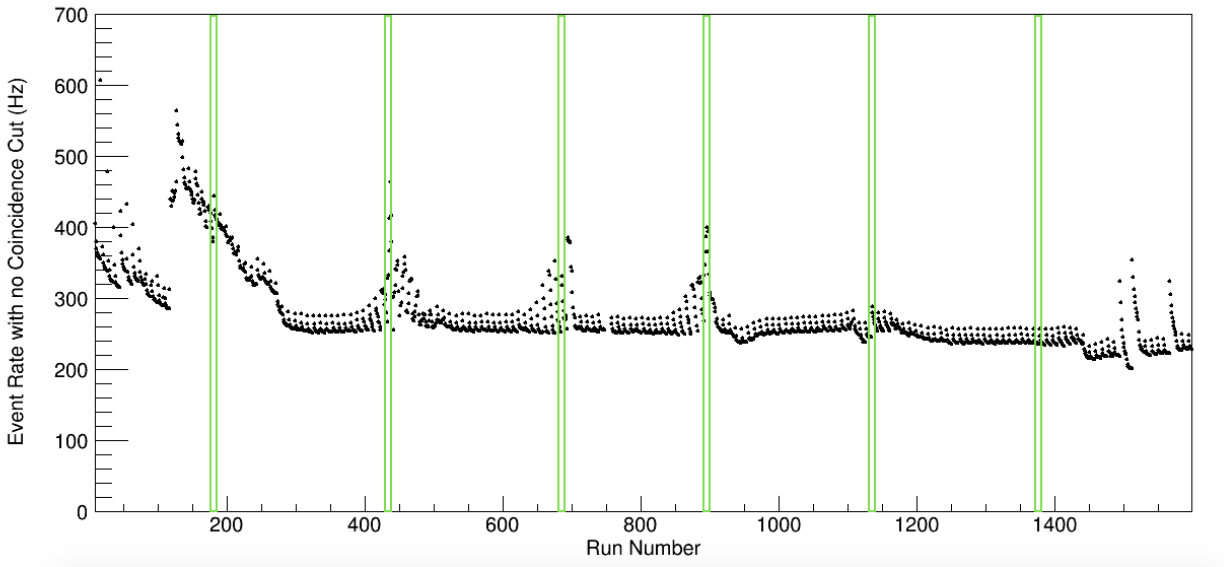

Figure 15: Total Event Rate for Runs 0009-1599 (August 2014 - March 2015).

I have depicted in green rectangles the full moon phases that occur approximately every 29-30

days. The last two phases you see that the rate does not change substantially. This is because those phases occurred in January and February and in Minnesota everything ices and snows over at that time. Thus, the snow and ice have covered the lake during these two phases and we don't have any substantial change in the background rate of the detector.

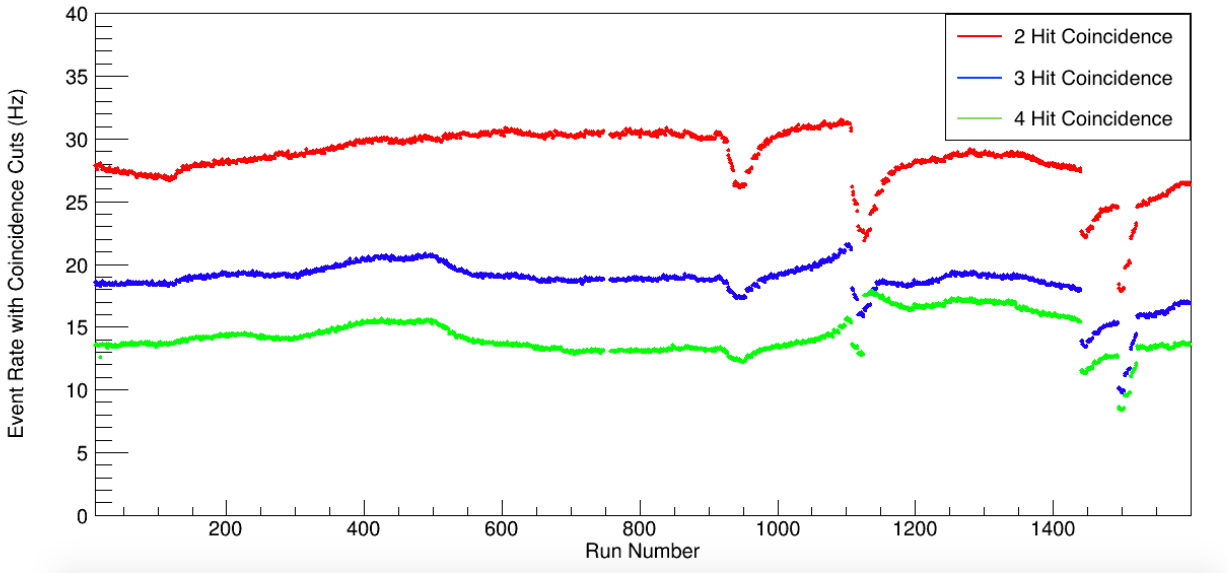

Figure 16: Event Rate versus the Event Time Window for runs 0009-1599 with various coincidence cuts.

As you can see from Figure 16 there are substantial dips in the event rate starting at approximately run 925 which is approximately early December or late November 2014. The second dip occurs in early January, the third dip is in mid February and the fourth dip a few days later. In the middle of February it was seen that there was a lot of the black sludge and debris in the filters when they were changed at the pit site. This could correspond to the two dips in the data in the middle of February.

6 CHIPS-M Event Display

My individual pursuit was to create an event display for CHIPS-M. An event display is a visual representation of the group of hits (deemed an event) in the detector. In my event display, the size of the sphere represents the size of the charge of the hit and the color of the sphere represents

the hit time in the detector.

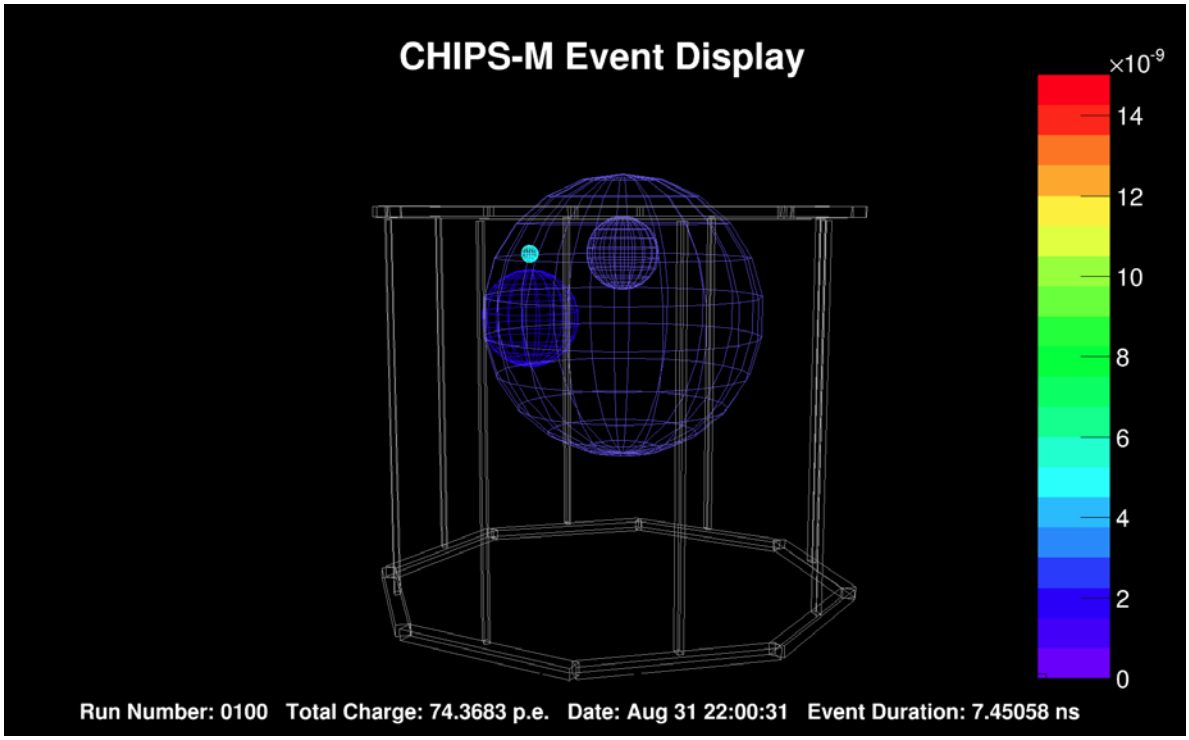

Figure 17: CHIPS-M Event Display

In Figure 17 you can see the general trajectory of the incoming particle. You have the largest hit at the bottom right DOM (the largest sphere) and as time progresses the charge gets smaller and it travels up and to the left. The light blue DOM is the last DOM hit and thus has the smallest integrated charge. It is not obvious what the source of the light comes from in this event display because the charges are not abnormally large as you would expect to see from a cosmic event.

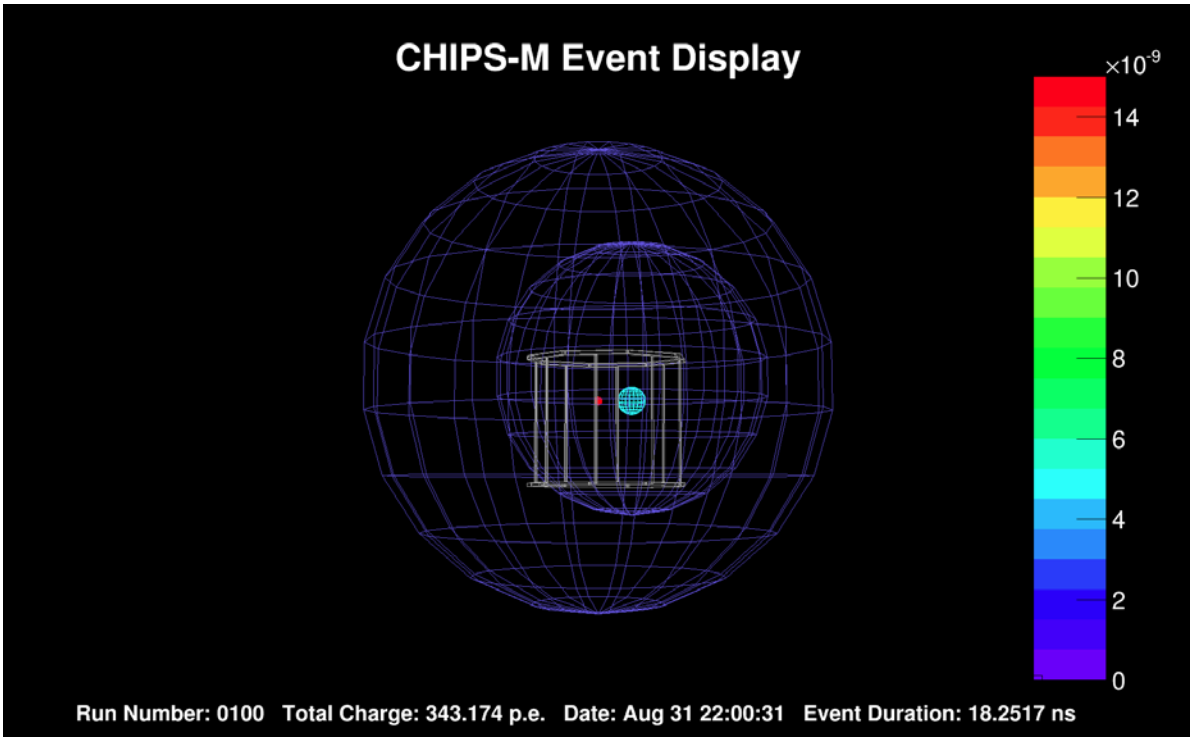

Figure 18: CHIPS-M Event Display

In Figure 18 we have a large downward moving light source. We could have evidence of an accidental grouping with the bottom left red sphere. This late firing could indicate that this event has grouped a small single background event in with it. The size of the charges are very large compared to background charges, so this could be an actual cosmic event interacting in our detector.

7 Conclusion

From analyzing the data from the first 90 runs from the CHIPS-M detector, we have shown that the optimal time window to group events is at 15 ns. With this time window we can be sure that we are minimizing the noise from the background single events. I worked with approximately 9 months of data over the past semester and have developed a thorough understanding of how this detector collects data. Even though we did not find an actual neutrino beam event in this detector, it was unlikely at the start of this program that the CHIPS-M module would do so. We now understand a lot of the background noise involved in this project and understand how to build

such a detector. A larger prototype is now underway to be constructed soon CHIPS-10 (a 10 kton water cherenkov detector). I will be traveling back to Minnesota this summer to bring CHIPS-M back out of the water and run a lessons learned session with my colleagues from the past year. The detector will be retrofitted with new PMTs and electronics and sank in the pit again to take data for another year. Together, hopefully we will be able to better understand how to build an underwater neutrino detector.

References

[1] Binkley, S. (2012, October 10). *Neutrino. History of a unique particle.* Retrieved April 15, 2015, from http://arxiv.org/pdf/1210.3065v1.pdf

[2] *Bioremediation for Sulfate Removal in Minnesota Mining Waters.* Bioremediation for Sulfate Removal in Minnesota Mining Waters. N.p., n.d. Web. 13 Feb. 2015. http://www.nrri.umn.edu/default/pt.asp?id=1723.

[3] CHIPS Internal Technical Note HEPDocDB-doc-321-v2. Retrieved April 17, 2015, from http://nile.hep.utexas.edu/cgi-bin/DocDB/ut-numi/private/DocumentDatabase

[4] Discovery of the Muon-Neutrino. (n.d.). Retrieved April 14, 2015, from https://www.bnl.gov/bnlweb/history/nobel/nobel_88.asp

[5] F. Reines and C. L. Cowan. *Detection of the free neutrino.* Phys. Rev. 92 (1953) 830-831.

[6] Fukuda, S. et al. (2001) *Physical Review Letters*, 86, 5651.

[7] Fukuda, Y. et al. (n.d.). Evidence for oscillation of atmospheric neutrinos. Retrieved April 17, 2015, from http://www-sk.icrr.u-tokyo.ac.jp/sk/pub/nuosc98.submitted.pdf

[8] G. Danby et al., Phys. Rev. Lett. 9 (1962) 36-44.

[9] Griffiths, D. (2008). Introduction to elementary particles (2nd, rev. ed.). Weinheim, Germany: Wiley-VCH.

[10] *Hydrogen Sulfide.* Wikipedia. Wikimedia Foundation, n.d. Web. 13 Feb. 2015. http://en.wikipedia.org/wiki/Hydrogen_sulfide.

[11] J. Beringer et al. (Particle Data Group), *Section 27: Passage of Particles through Matter*, Phys. Rev. D86 (2012).

[12] J. Beringer et al. (Particle Data Group), *Section 28: Particle Detectors.* Phys. Rev. D86 (2012).

[13] K.A. Olive et al. (Particle Data Group), *Section 13: Neutrino Mixing.* Chin. Phys. C, 38, 090001 (2014).

[14] Kruppke D. (2007) *On Theories of Neutrino Oscillations: A Summary and Characterization of the Problematic Aspects* (Diploma Thesis).

[15] L. Brown, *The Idea of the Neutrino*, Physics Today 31(9), 23 (1978).

[16] M. Perl (SLAC)., *The Discovery of the tau lepton.*, 79-100 (1992).

[17] Melissinos, A., Napolitano, J. (2003). The Statistics of Nuclear Counting. In Experiments in modern physics,. San Diego: Academic Press.

[18] Neutrino Detection. (n.d.). Retrieved April 15, 2015, from http://t2k-experiment.org/neutrinos/neutrino-detection/

[19] *Neutrino Oscillation Phenomenology.* In Neutrino Oscillation: Present Status and Future Plans, edited by Patricia Vahle and Jenny Thomas. 2008.

[20] P. Adamson et al., *CHerenkov detectors In mine PitS (CHIPS) Letter of Intent to FNAL*, 23 September, 2013.

[21] P. Adamson et al., *CHerenkov detectors In mine PitS (CHIPS) RD Proposal*, 30 December, 2013.

[22] Parke, S. (2013, October 22). Neutrinos: Theory and Phenomenology. Retrieved April 15, 2015, from http://arxiv.org/pdf/1310.5992.pdf

[23] R. Abbasi et al. (IceCube Collaboration), Nucl. Instrum. Meth. A601, 294 (2009), arXiv:0810.4930.

[24] *Stainless Steel.* Wikipedia. Wikimedia Foundation, n.d. Web. 13 Feb. 2015. http://en.wikipedia.org/wiki/Stainless_steel.

[25] *Sulfate-reducing Bacteria.* Wikipedia. Wikimedia Foundation, n.d. Web. 13 Feb. 2015. http://en.wikipedia.org/wiki/Sulfate-reducing_bacteria.

[26] *Why Doesn't Stainless Steel Rust?* Scientific American Global RSS. N.p., n.d. Web. 12 Feb. 2015. http://www.scientificamerican.com/article/why-doesnt-stainless-stee/.

XSJJ-7-CCP DOM Submarine Connector with 9207Belden Twin-axial Cable Underwater Splice, 9-Pin Serial Download Cable Splice, and Twin-axial Repair Splice Manual

B. Kriesten *A. Laundrie †

Abstract

To prepare for the CHIPS-M DOM deployment, we must have cables which will run from the DOMs in the CHIPS-M detector to the shed on shore. The cables and the connectors will be underwater necessitating an underwater splice to ensure that there is minimal signal attenuation. This splicing technique was developed by Andrew Laundrie of the Physical Sciences Lab, University of Wisconsin. To connect the cable to the DOM hub we need a db9 connector on the end of the twin-axial cable. The procedure for the 9 Pin splice is described in this manual as well. To prepare for any repairs that must be made to the cable, a procedure was also developed for splicing two ends of the twin-axial cables as well. Several tests were performed on these cables such as a DOM communications test, a short MOAT test, and a high POT test. For more information on these tests, see the appendices.

Materials/Tools

Below is a detailed list of the items needed for a single underwater splice and a single 9-Pin splice

* *Department of Physics, The College of William and Mary: Williamsburg, VA. 23187*

- Resin Core Solder #500G, Type: 370 flux 5 Core, Diameter: .56mm
- High Gel Reenterable Encapsulant 3M #8882
- 3M Scotch #69 Glass Cloth Electrical Tape Class "H" Insulation
- XSJJ-7-CCP DOM Submarine Connector
- Belden9207 Twin-axial Cable
- Linerless Rubber Splicing Tape #130C
- Heat Shrink Tubing Sizes: $\frac{1}{16}$ in., $\frac{3}{16}$ in., $\frac{1}{2}$ in., $\frac{3}{4}$ in., 1 in.(3:1 ratio with adhesive lining)
- Modified X-acto knife
- Measuring Tape
- Heat Gun
- Wire Cutters
- Wire Strippers
- Scissors
- Electrical Tape (black)
- Kim Wipes
- Soldering Iron
- 2 x 600mL beakers
- 5 x 30mL beakers
- Jacket Stripper
- Pipettes
- Rubber Gloves

- Loupe (10x magnification
- Plastic Stirring Stick

Underwater Splice Procedure

Below is an illustrated enumeration of the various steps in underwater splicing the XSJJ connector with the 9207 Twin-axial cable.

1. Cut heat shrink tubing in the following lengths:

   1in. at length 8 in. (large) - $\frac{3}{4}$in. at length 14 in. (medium) - $\frac{1}{2}$in. at length 12 in. (small) - $\frac{3}{16}$in. at length 2x1in. and at 2x5in. (x-small)

   Slide heat shrink tube over the end of the twinaxial cable in the same order (1 large, 1 medium, 1 small). These shrink tubes will be used at the end of this procedure but need to go on now to ensure that they can be used later.

2. Using the modified X-acto knife, strip off the polyethylene black jacket 8in. by scoring a line vertically then peeling the jacket back. Use wire cutters to cut the jacket around the base of the score.

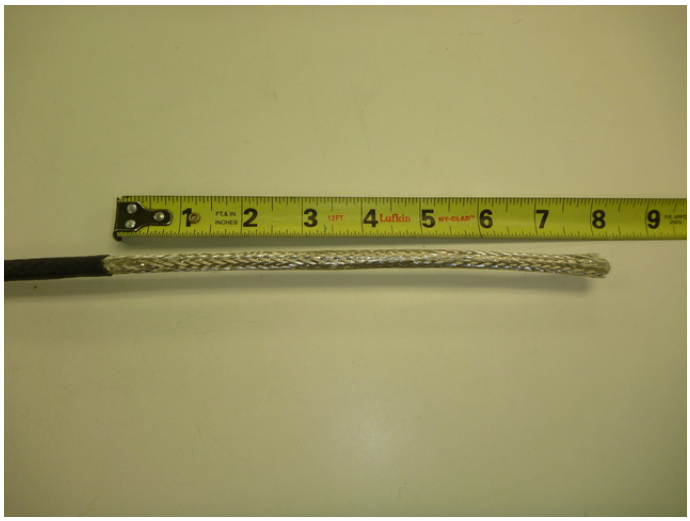

3. Roll down the wire mesh shielding and tape it to the cable so that it is out of the way. Be careful when doing this, if the wire mesh becomes tangled then you must cut at the base of the score and start from step 1 again.

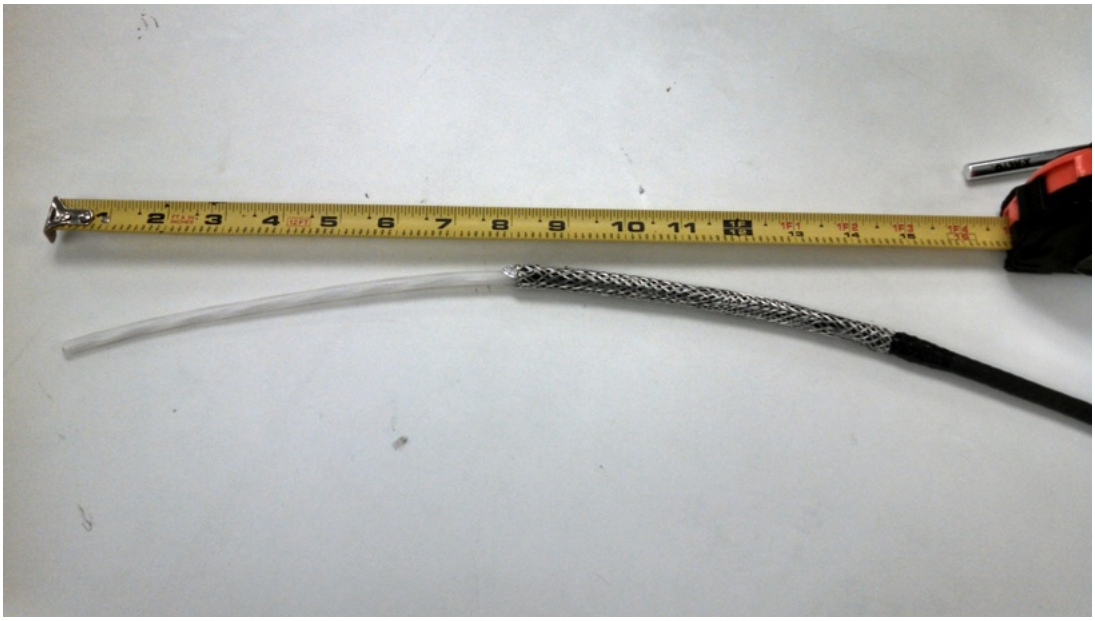

4. Remove the foil shielding from the inner polyethylene jacket.

5. Remove the white polyethylene jacket using a Jacket Stripper. Leave 1 in. of the jacket from the wire mesh end and remove the rest.

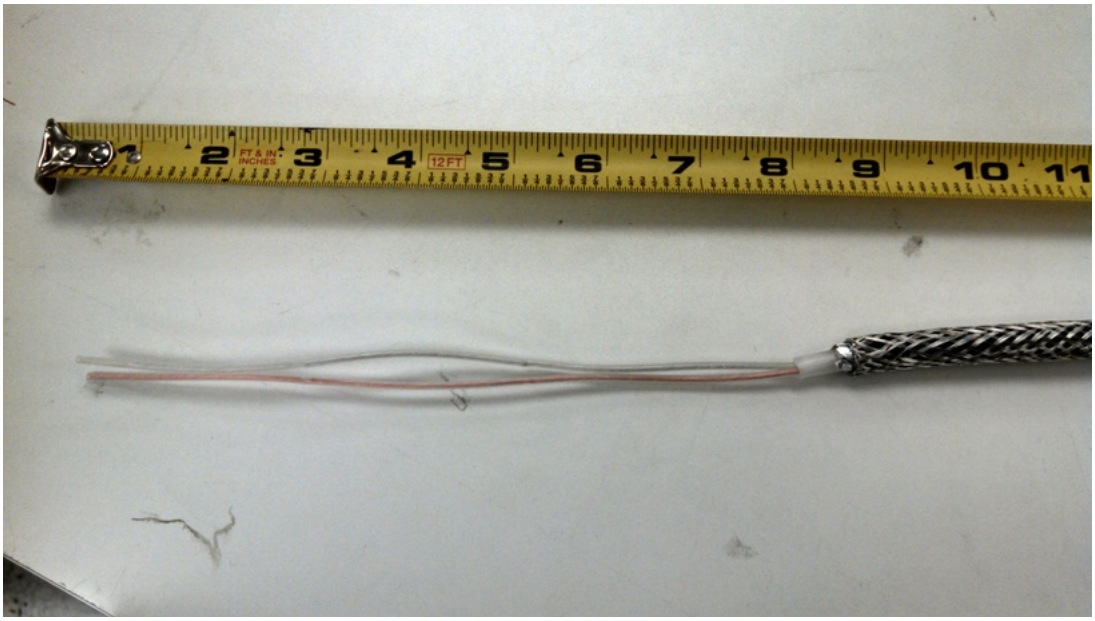

6. Cut the wires 7 in. from the wire mesh shielding.

7. Check the wire insulation for holes or other damage with the Loupe.

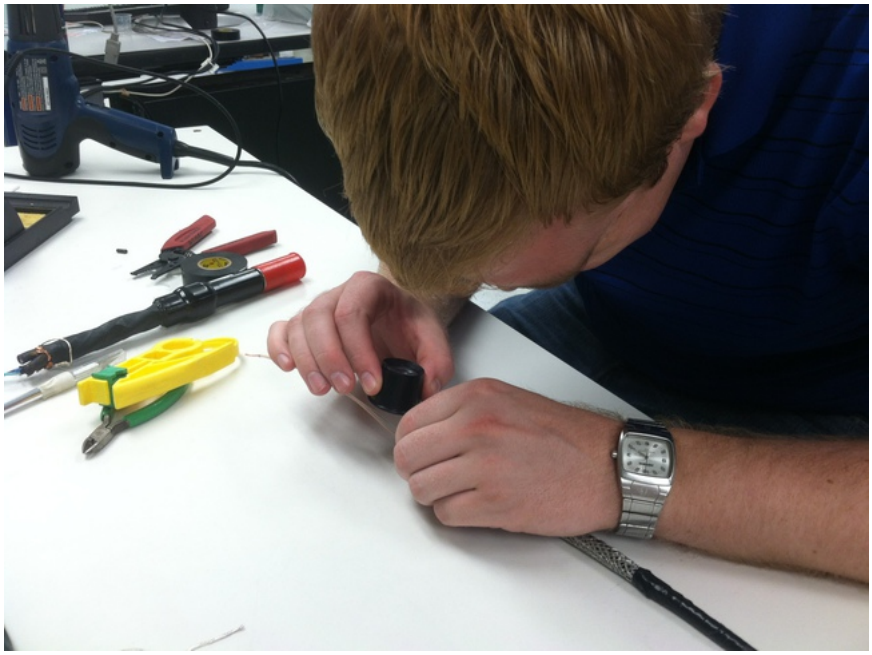

8. Strip the two inner wires $\frac{3}{8}$ in. from the tip to ensure a proper surface in which to solder.

9. Slide the two x-small 1in. length shrink tubing pieces over the DOM connector ends. One piece for each wire coming from the DOM connector.

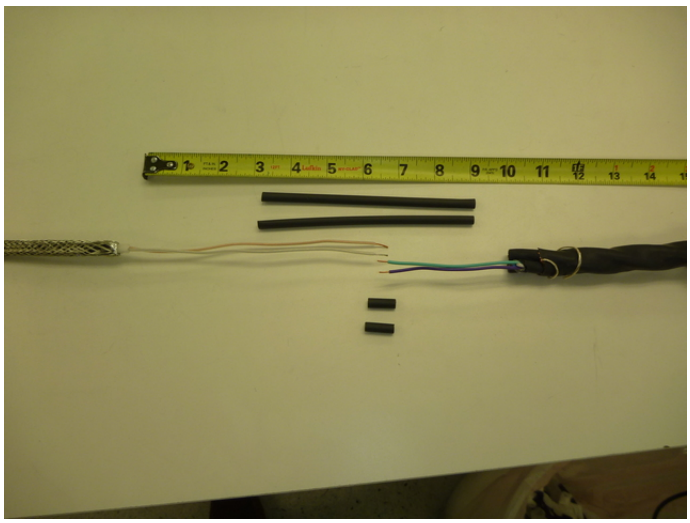

10. Slide the two x-small 5in. length shrink tubing pieces over the twin-axial cable ends. One piece for each inner wire.

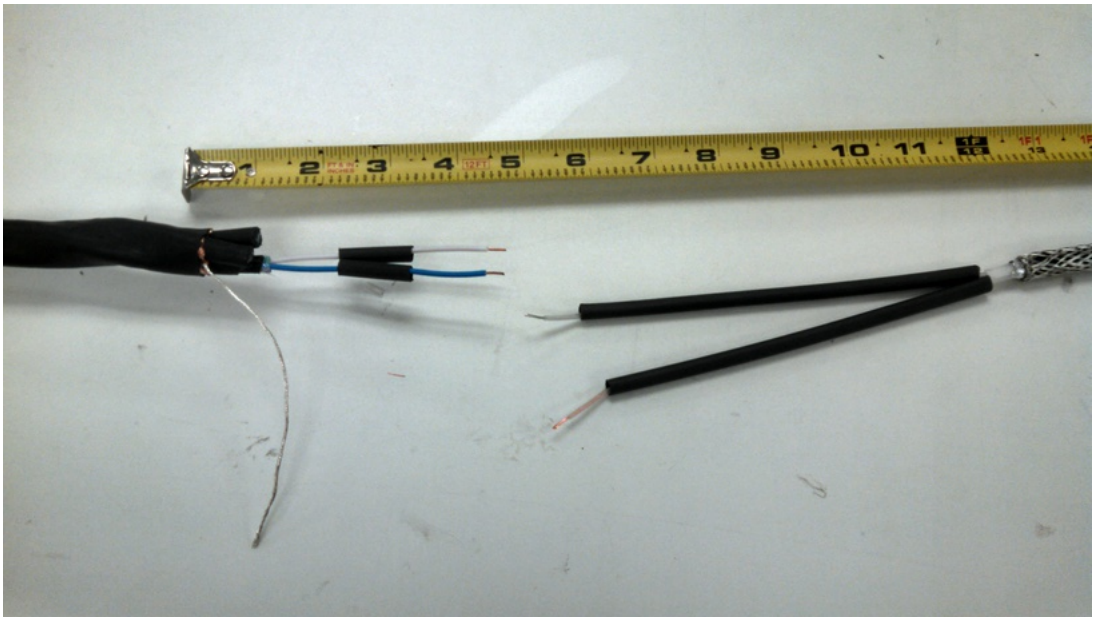

11. Splice the twin-axial cable inner wire with the corresponding XSJJ connector wire (see color coding chart for the color scheme). Make sure there is a definite connection and that it is strong enough to support itself (will not fall apart when you let go of it). This is a very crucial step in this procedure.

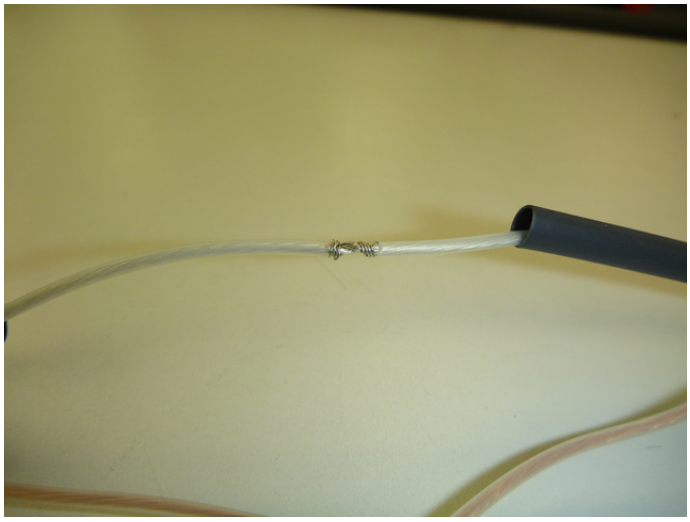

12. Solder the connection of 1 of the splices from step 7. Make sure that the connection does not move when you are finished soldering and the solder is cooling. NOTE: Do not keep the soldering iron on the wires for too long or you will melt the insulation. This causes a mess and is very sloppy work.

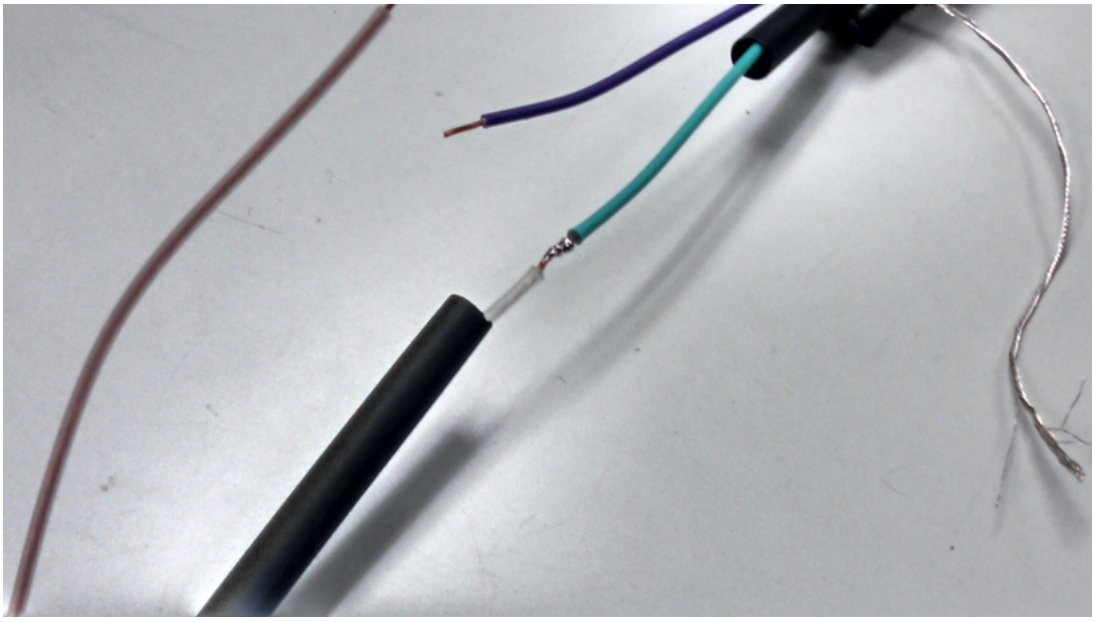

13. Center the x-small 1in. piece of shrink tubing from step 9 over the soldered splice. Use the heat gun to shrink the tubing to seal it, starting from the middle and working out towards one end. Repeat the process for the other end and allow time for the shrink tubing to cool.

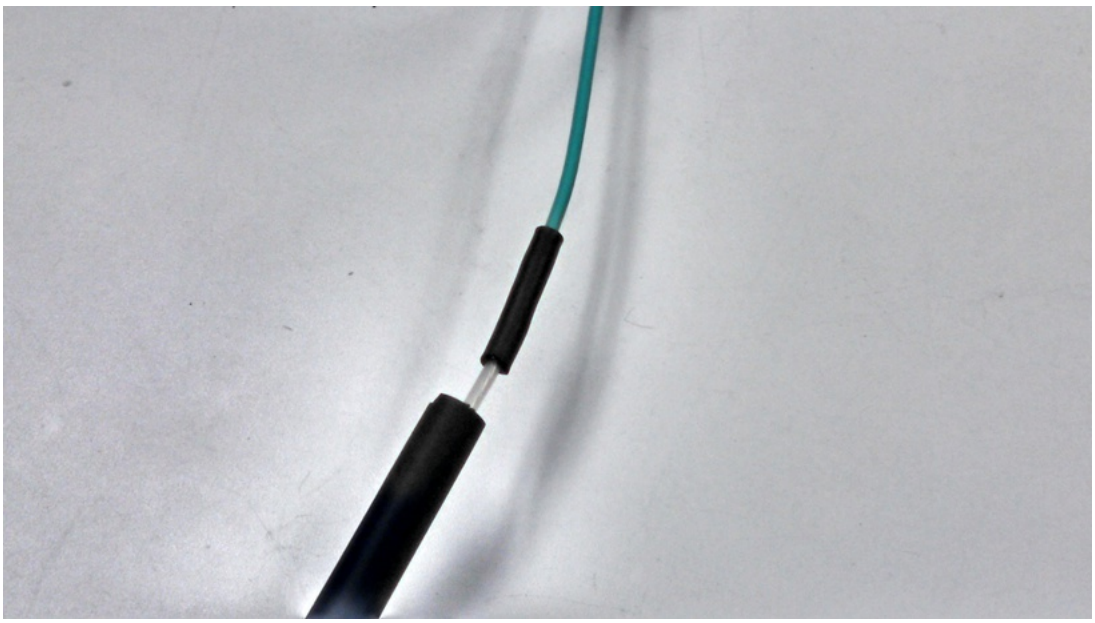

14. Center the x-small 5in. piece of shrink tubing from step 10 over this connection and use the heat gun to seal it. Start from the center and work your way out towards the ends to ensure proper watertight sealing.

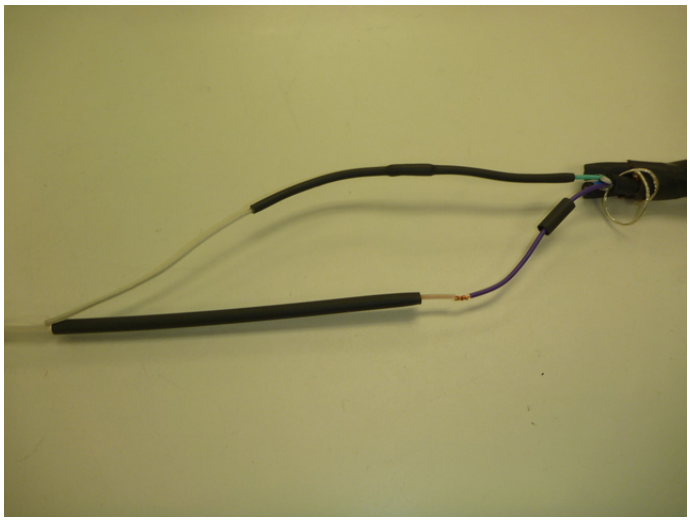

15. Repeat steps 13 and 14 for the second inner wire of the twin-axial cable.

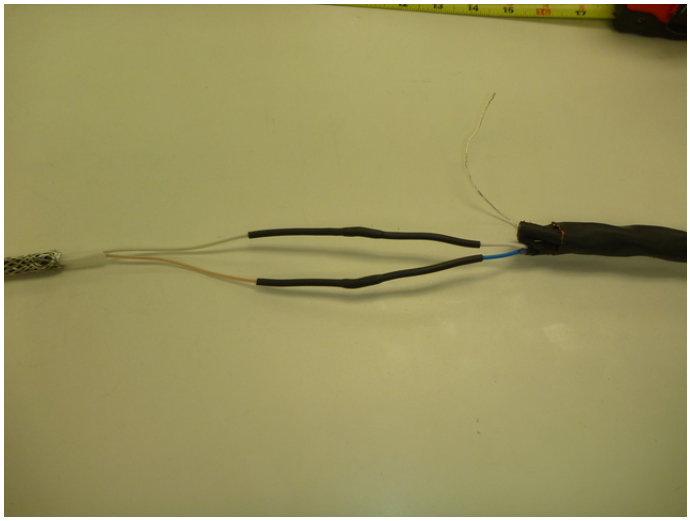

16. Connect a spare test cable to the XSJJ Connector and run an electrical conductivity test with the DVM. This ensures that we do not have any shorts in our splice.

17. Hang up the twin-axial cable with the XSJJ Connector splice so that it is easier to pour the high gel down the length of the cable. Cover the end of the cap with Kimwipes and some electrical tape to ensure that the XSJJ Connector does not get the high gel into the connection.

18. Slide down the first sleeve of the shrink tubing (the $\frac{1}{2}$ in. diameter piece) down the length of the twin-axial cable until it reaches the end of the connector.

19. Shrink the tubing at the very bottom as little as possible, just enough to ensure a gel proof seal.

20. Pour the contents of the high gel into two sealable containers (one packet of gel for each container, DO NOT MIX THEM YET). Pour 15mL of each of the gels into a small beaker

and stir with a plastic dowel.

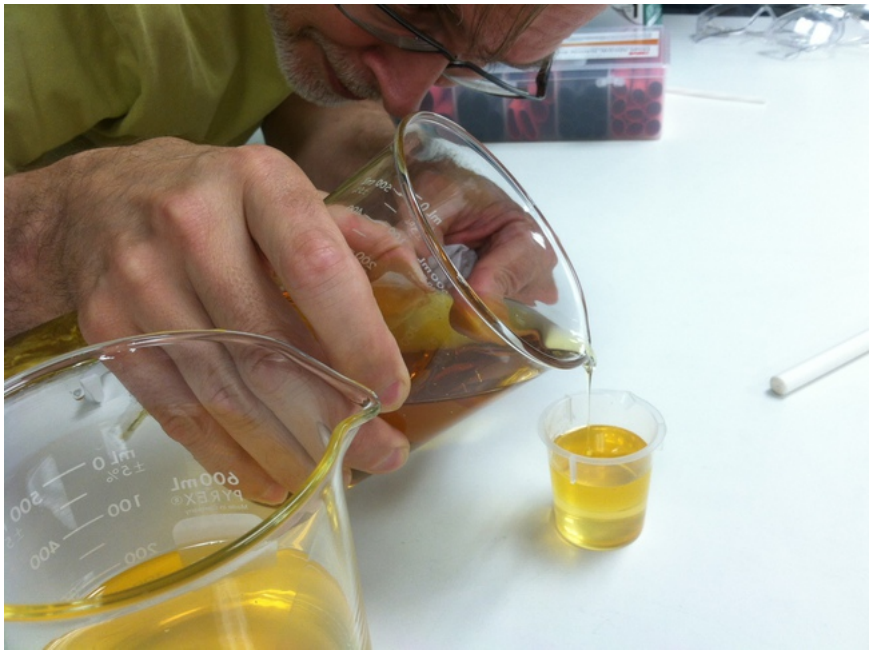

21. Pour approximately 5mL of the high gel down the length of the tubing to ensure that our connection does not have water in it. Gently massage the gel down the tube to ensure that it drips down the entire length.

22. Using the heat gun, shrink the tubing starting from the bottom and working your way up to the top. Watch for the gel leaking out the top of the tubing. If this occurs, use the pipettes to remove the excess gel. Continue this process until the tubing is completely sealed.

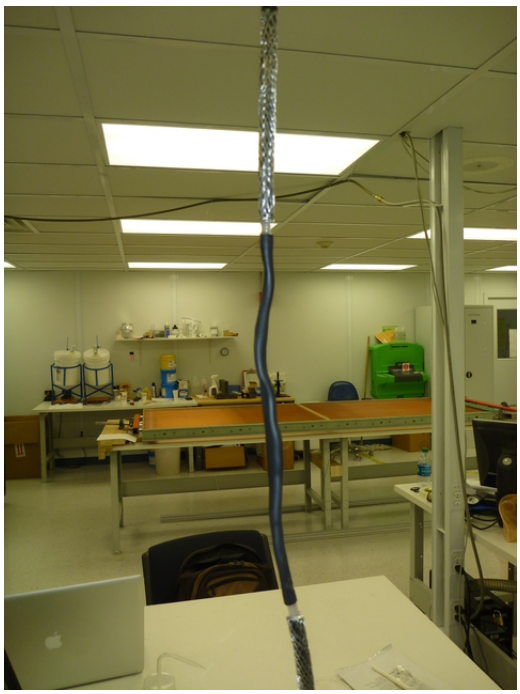

23. Slide the wire mesh shielding down over the tubing and connect it with the drain wire from the XSJJ connector. IMPORTANT: Ensure that the tension of somebody pulling the wire resides in the drain wire and not in the 20 gauge inner wires.

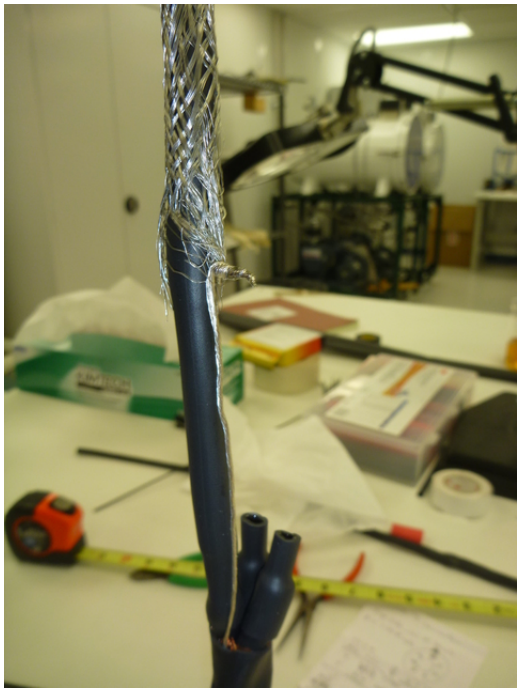

24. Solder the connection between the drain wire and the wire mesh tubing. Be careful to not melt the polyethylene jacket with the soldering iron.

25. Slide down the $\frac{3}{4}$ in. tubing over the wire mesh all the way down to the connectors.

26. Repeat steps 18-20

27. Place two pieces of the $\frac{1}{2}$ in. tubing over the unused quad cables on the connector and heat shrink them. Then seal with a bit of high gel encapsulant to ensure that there is a water proof seal.

28. Slide down the 1 in. tube down the twin-axial wire until it is 2 in. overlapping the XSJJ connector.

29. Repeat steps 18-20 but with approximately 10 mL of the high gel.

30. Allow several hours to ensure that the gel has set.

31. FINISHED!

9-Pin Splice Procedure

1. Cut the 9-pin serial download cable in half at the 6 ft. length. We will be using the male side for our purposes; however, in order to perform the High Potential test (see Appendix) we will need the female end, so do not throw it away.

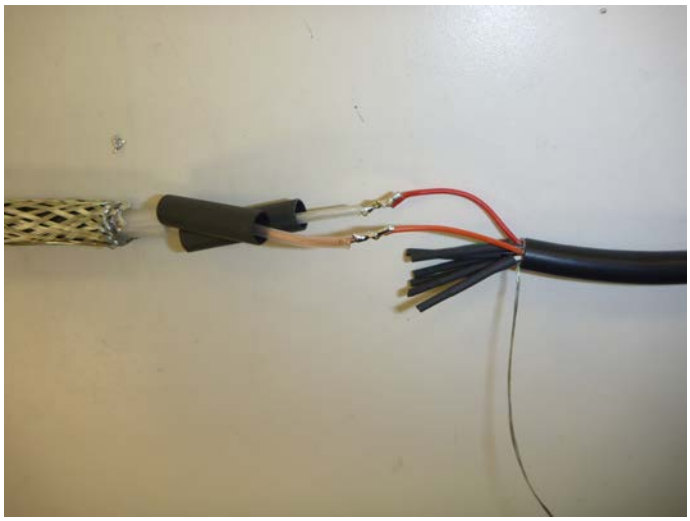

2. Cut approximately 8 in. of the $\frac{1}{2}$ in. shrink tubing and place it on the 9-pin cable side. We will use this tubing at the very end of our procedure.

3. Remove the foil inner shielding and expose the 10 wires inside.

4. Using a Continuity Tester, locate all of the pins and their corresponding wires. We are looking for pins 4 and 5 and their matching wires. Also maintain the non-insulated wire (the drain). The other wires can be cut back to $\frac{1}{2}$ in.

5. Cut 7 pieces of the $\frac{1}{16}$in. tubing in 1 in. lengths.

6. Put the tubing over each of the unused 24 gauge wires and heat shrink them to seal the wires.

7. Cut wires 4 and 5 to 2in. in length and strip them $\frac{3}{8}$ in. from the end.

8. Cut 2 pieces of $\frac{3}{16}$in. tubing at 1 in. lengths and put the tubing over wires 4 and 5, far enough away so that the solder will not interfere with them. We will now work on the twin axial cable.

9. Strip the polyethylene jacket of the twin-axial cable 4 in. from the end and remove it.

10. Pull the wire mesh shielding back and tape to the twin axial cable using black electrical tape.

11. Cut the polyethylene inner jacket back to $\frac{3}{8}$ in. from the wire mesh shielding.

12. Cut the inner 20 gauge wires so that they are 2.25 in. from the wire mesh shielding.

13. Strip the inner wires $\frac{3}{8}$ in. from the ends to ensure proper solder connection. We are now ready to connect the two cables.

14. Using the color scheme, splice the two wires together ensuring a good connection.

15. Solder the splice, make sure that the solder penetrates the splice and does not move. This is a very crucial step in the process.

16. Place the 1in. lengths of heat shrink tubing over the soldered ends. Using the heat gun, shrink the tubing.

17. Beginning $\frac{1}{4}$ in. on the 9-Pin Serial Download cable, use the glass cloth tape to provide support. Work your way up in a half lapping motion until you are well over the soldered connection.

18. Twist the drain wire to ensure that it will not unravel, and solder the tip of it.

19. Begin to pull down the shielding mesh. Hold the drain wire and pass it through one of the holes in the mesh and finish pulling down the shielding.

20. While making sure that all of the tension is in the drain wire and not the wire mesh shielding when pulled, solder the connection between the drain wire and the mesh shielding.

21. Tape the entire length (approximately 7 in.) with the glass cloth tape. Use a half lapping motion to ensure stability and build up of strength.

22. Move the 8in piece of shrink tube from step 2 over the glass cloth tape and cover fully. Using the heat gun shrink the tubing.

Repair Splice Procedure

1. Strip the outer black polyethylene jacket of the twin-axial cables at 6in. for each cable. Do this by lightly scoring the jacket with the modified X-acto knife and then peeling the jacket back. Use wire cutters to trim around the base and remove the jacket completely.

2. Peel back the foil shielding surrounding the wire mesh shielding, cut it back to where the jacket was cut.

3. Pull back the wire mesh over the twin-axial cable and tape it to the jacket using electrical tape so that it is out of the way.

4. Strip off the inner white polyethylene jacket using a modified jacket stripper. This will have to be done in multiple steps as it is rather difficult to come off. Use smaller cuts and then bend the wires at the cuts to ensure that the cut has penetrated through the jacket.

5. Check that the two inner wires' insulation have not been damaged.

6. Repeat steps 1-5 for the second twin axial cable.

7. For one cable, cut the two inner wires so that they are 3.5in. from the wire mesh shielding.

8. Strip both sets of inner wires $\frac{3}{8}$in. from the tip of the wires.

9. Cut 10in. and 15in. of the $\frac{1}{2}$in. tubing and place them over one end of the cable, out of the way so that we can still work on the splice. The 15 in. piece should go on first as it will be the last one we use.

10. Cut 2 1in. pieces, and 2 6in. pieces of the $\frac{3}{16}$in. tubing and place one set over each of the inner wires.

11. Connect the wires with the corresponding colors (copper to copper and silver to silver)

12. Solder the two connections together. You need to provide enough heat and solder such that the solder penetrates the splice, but not too much as to melt the insulation of the wires.

13. Place the 1in. tubing over the connection and heat shrink the tubing so that we get a nice seal.

14. Center the 6in. tubing over the other heat shrink and use the heat gun to shrink the tubing.

15. Repeat steps 11 and 12 for the second inner wire.

16. Hang up the twin axial cable so that we can have better access to it with the high gel encapsulant.

17. Slide the 10in. piece of $\frac{1}{2}$in. shrink tubing over the shielding and heat shrink the very bottom in order to ensure a gel proof seal.

18. Fill the tubing up with 5mL of the high gel encapsulant, massage the gel down into the splice.

19. Heat shrink from the bottom up, using the pipettes to clean up any residual gel that may leak out.

20. Slide the two wire mesh shielding down so that they meet. Form a strand bunch on either side of the mesh for both sets of shielding. These strands we will then twist together to form a splice.

21. Solder the two splices from above on either side of the cable. Be careful not to melt the polyethylene outer jacket. When the solder has cooled, bend the two points down to prevent any sharp edges.

22. Slide the 15in. tubing over the wire mesh and shrink the bottom of the tube to ensure a gel proof seal.

23. Repeat steps 18 and 19

DOM Optical Test

Connecting the DOM to the XSJJ Connector

1. Turn off the DOM High Voltage Power Supply.
2. Unspool enough cable to reach the connector.
3. Loosen the red ratchet strap and pull up the black curtain around the DOM tank. Pull out the DOM connector piece enough so that you can connect the XSJJ Connector to the DOM.
4. Connect the XSJJ Connector to the DOM by having the cable run under the red ratchet strap, ensuring that the black curtain will come down again.
5. Pull the black curtain over the apparatus again and tighten the red ratchet strap.
6. Plug the Db9 connector in the hub 3^{rd} from the left. This DOM is called 10A.
7. Turn on the high voltage and turn off the lights in the room.

Running the Laser Script

1. In a Terminal window run:

```
$ssh testdaq@hawc-hub psswd: *******
$cd abscal/daq/omicron
$on all
$iceboot all
$nohup ./pulserScan.py run000 ### "Any comment for future recognition"
abscal-Glutta-bigpulses biglaserpulses &
```

2. In a new window run:

```
$ssh -X testdaq@hawc-hub
$cd abscal/daq/omicron
$java -Xmx1000m -jar ~/domdisplay.jar -S DomDOM 0 .5 max
```

3. Choose the run number that you specified earlier.
4. We want to look at the Δt histogram.
5. Limit Δt such that it is at 200 ns.
6. Zoom into the second peak around 120 ns.
7. Set the number of bins to approximately 20.
8. Fit the histogram with a Gaussian, and look at the fit sigma. We want a fit sigma of approximately 1.
9. Go to Window -> Quit
10. In the first Terminal window type:

```
$off all
```

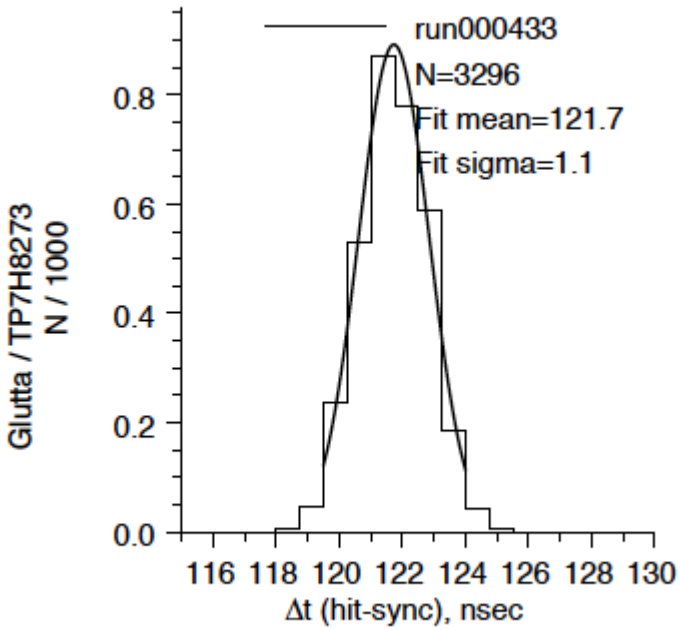

Short Moat Test

The short moat test is a test of the communications with the DOMs.

Output looks like:

MOAT: Started at Thu Jul 3 19:51:07 2014 CVS Id: moat,v 1.29 2007/11/14 04:41:49 jacobsen Exp

MOAT test iteration 0...

MOAT: Starting /usr/local/bin/stagedtests.pl -b -t 120 -x -d 10 -s st.in Stagedtests.pl: SUCCESS.

MOAT: Starting /usr/local/bin/stagedtests.pl -t 120 -a -v -d 10 st.in -a Stagedtests.pl: SUCCESS.

MOAT: Starting /usr/local/bin/stagedtests.pl -t 120 -d 10 st.in Stagedtests.pl: SUCCESS.

MOAT: Starting /usr/local/bin/stagedtests.pl -t 120 -d 10 -a st.in Stagedtests.pl: SUCCESS. MOAT: Test iteration 0 succeeded. MOAT: Powering off all DOMs.

Electrical Conductivity Test

To test the electrical conductivity, we used a db9 connector (female) with a short section of cable (6ft), also known as a pigtail. We stripped the pigtail and found which wires were connected to pins 4, 5, and the metal shroud (bare drain wire).

Pin 4 on the DB-9 connects to Pin 5 on the XSJJ (DOM) connector.

Pin 5 on the DB-9 connects to Pin 4 on the DOM connector.

The shield on the DB-9 connector connects to Pin 1 of the DOM connector.

We used the DVM to test whether there was conductivity between each of these connections. So Pin 5 on the XSJJ should conduct with Pin 4 on the DB-9, etc.

Appendix B: Filling and Circulation Scheme

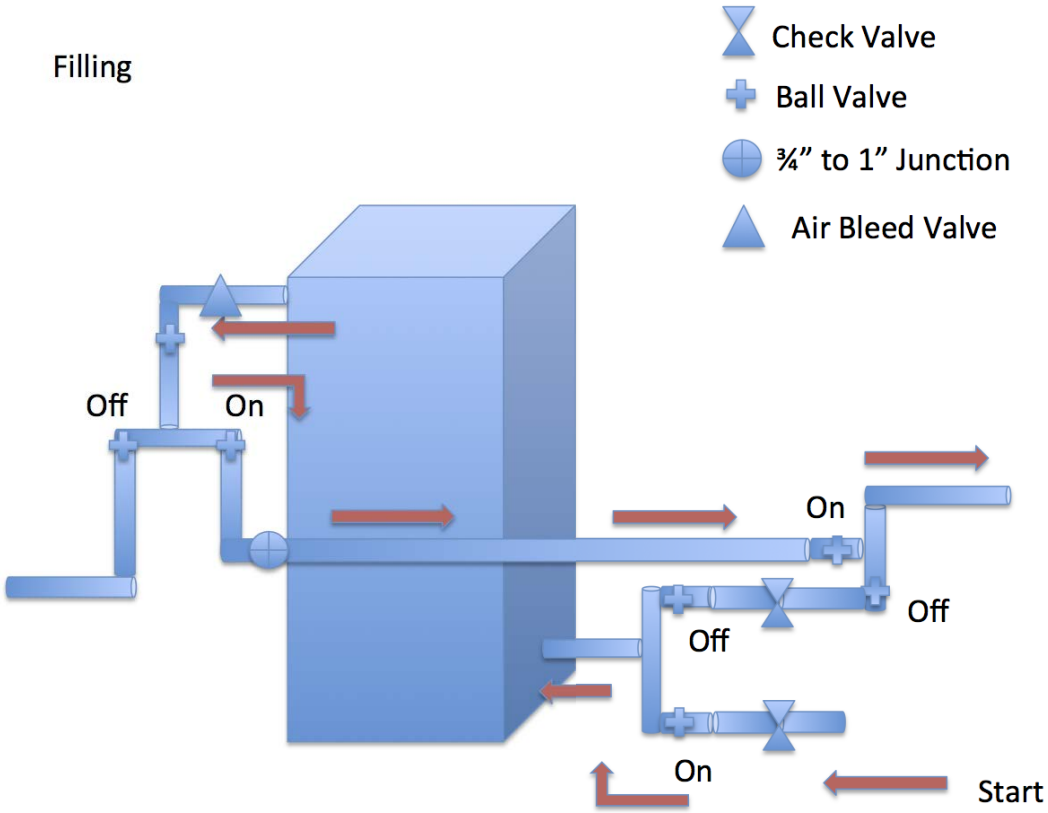

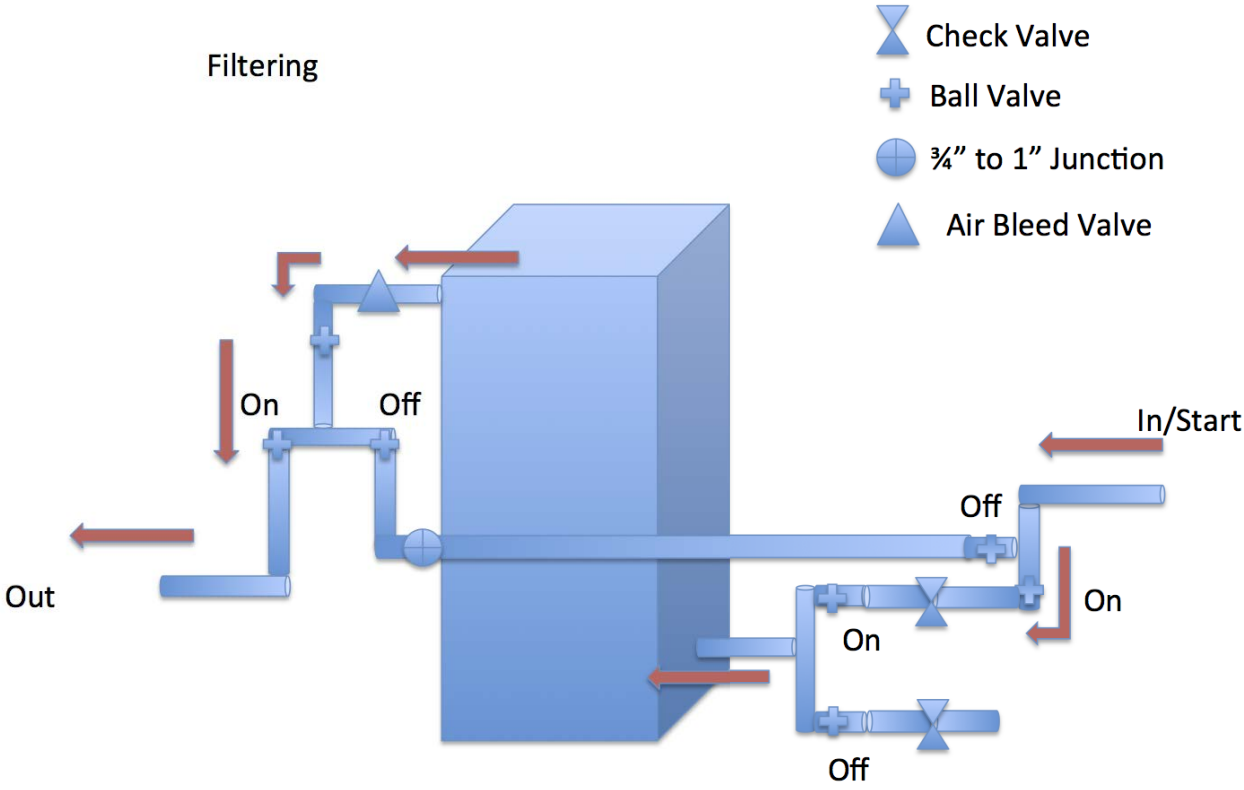
Filtering
Check Valve
Ball Valve
¾" to 1" Junction
Air Bleed Valve
On
Off
In/Start
Off
Out
On
On
Off

Appendix C: Description of the Variables Used in the Code

CkovHitTree Variables

Variable	Type	Summary
domID	string	The name of the DOM
gpstimesec	double	The whole seconds portion of the gps time stamp as a whole number
gpstimefrac	double	The fraction of a second portion of the gpstimestamp as a decimal
t50	double	The time it takes to interpolate half of the charge in the DOM in nanoseconds
gpstimediff	double	The difference in the time from one hit to the next subsequent hit in gps time order
gpstimediff_pmt	double	The difference in time from one hit to the next subsequent hit in the same pmt
qtotal	double	The total charge integrated on the DOM
gpstimediffpecut	double	The time difference between one hit and the next subsequent hit in gps time order above 2.5 p.e.
gpstimediffpecut_pmt	double	The time difference between on hit and the next subsequent hit in the same pmt above 2.5 p.e.

CkovEventTree Variables

Variable	Type	Summary
same_pmt_hit	double	A boolean variable that checks if the event has a DOM that has fired more than once in the event
start_time	double	The gps time of when the event started (with t50 included)
stop_time	double	The gps time of when the event stopped (with t50 included)
delta_t	double	The total time of the event (calculated by subtracting stop_time from start_time
qtotal	double	The total charge of the entire event
num_hits	double	The total number of hits in the event
spill_time	double	Empty Variable (could eventually be used to track the spill time of the NuMI beam line
CkovHits	vector	A vector containing all of the CkovHit class instances
elapsed time	vector	A vector containing the elapsed time of each hit in the event for time ordering purposes

CkovEventSum Variables

Variable	Type	Summary
run_num	int	The run number of the file
rawdate_start	string	The raw start date and time as given by the gps time stamp
rawdate_stop	string	The raw stop date and time as given by the gps time stamp
start_month	int	The start month of the event file
start_day	int	The start day of the event file
start_hour	int	The start hour of the event file
start_min	int	The start minute of the event file
start_sec	int	The start second of the event file
start_year	int	The start year of the event file
end_month	int	The end month of the event file
end_day	int	The end day of the event file
end_hour	int	The end hour of the event file
end_min	int	The end minute of the event file
end_sec	int	The end second of the event file
end_year	int	The end year of the event file
total_hit	double	The total number of hits in the event file
sing_coinc	double	The number of single coincidence hits in the event file
doub_coinc	double	The number of double coincidence hits in the event file
trip_coinc	double	The number of triple coincidence hits in the event file
quad_coinc	double	The number of quadruple coincidence hits in the event file
run_time	double	The total time of the event file in seconds
start_time	double	The start time of the event file
stop_time	double	The stop time of the event file
cal_date	double	The calendar date of the event file
water_level	double	Empty Variable
tot_rate	double	The total event rate
sing_rate	double	The rate of single hit coincidence events

doub_rate	double	The rate of 2 hit coincidence events
trip_rate	double	The rate of 3 hit coincidence events
quad_rate	double	The rate of 4 hit coincidence events
sunrise_t	double	Empty Variable
sunset_t	double	Empty Variable
moonrise_t	double	Empty Variable
moonset_t	double	Empty Variable
sun_up	bool	Empty Variable